Fine Resolution Radar for Near-Surface

Layer Mapping

By

Rohit Parthasarathy

B.S., Electrical Engineering,

University of Kansas, 2002

Submitted to the Department of Electrical Engineering and Computer Science and the

Faculty of the Graduate School of the University of Kansas in partial fulfillment of

the requirements for the degree of Master of Science.

_____

Chair: Sivaprasad Gogineni

_____

Christopher Allen

_____

Glenn Prescott

_____

Date Thesis Accepted

1

ACKNOWLEDGEMENTS

ABSTRACT

It is estimated that sea levels have risen 4 to 8 m in the last century. Currently, there is much uncertainty regarding the contribution to this rise from melting ice sheets and glaciers. The key parameter in quantifying the ice sheets contribution is assessing their mass balance. The accumulation rate is a key parameter in computing the mass balance. Remote sensing techniques are required to reduce the uncertainty that currently exists in accumulation rate measurements due to sparse sampling of ice cores and pits.

A wideband FM-CW radar was developed to map the near-surface internal layers with high resolution. The radar operated at frequencies from 500 to 2000 MHz. With this bandwidth, the free-space resolution is 10 cm. We used a YIG oscillator in a Phase-Locked Loop configuration to obtain an extremely linear transmit signal. We leveled the power of the transmit signal using an Automatic Gain Control system. The entire radar fits inside one CompactPCI chassis.

We analyzed the effect of any amplitude variation and phase non-linearity in the transmit signal on the sideband performance of the IF spectrum. We also developed a simple phase-noise model for a YIG oscillator, and compared our model with the actual phase-noise performance of the YIG oscillator.

We tested the radar extensively in the laboratory and field. We obtained excellent internal layer mapping from the 2003 field experiment in NGRIP camp, Greenland and from the 2004 field experiment in Summit camp, Greenland. We are able to see internal layers to a depth of 200 m with fine resolution.

TABLE OF CONTENTS

LIST OF FIGURES

LIST OF TABLES

CHAPTER 1

INTRODUCTION

1.1 Reasons For Studying Glacial Ice

Due to the close proximity of the ocean and atmosphere, and because the heat capacity of the ocean is so large, ocean conditions, particularly the rising sea level, are a significant indicator of global climate change [1]. In the last one hundred years, sea level rise has been estimated to be between 4 and 8 inches [2]. The rise is in part due to thermal expansion, since warm water takes more space than cooler water. The average global surface temperature has also risen, by about 1.8° F over the last century, and this trend could continue. Some scientists believe the rise in global temperature is a result of increased greenhouse gases in the atmosphere, but irrespective of the cause, the consequences could be severe. A major concern is that a continued rise of global temperature will melt the polar ice caps and small glaciers, which would have devastating effects on humanity. Although small glaciers make up only 4% of the total land ice area, they may have contributed up to 30% of the sea level rise this past century because of rapid ice volume reduction due to global warming [3]. It is estimated that if the entire Greenland ice sheet were to melt, sea levels would rise by about 7 meters (23 feet). Such an occurrence would submerge coastal cities and displace a large population, since a large percentage of the world's population lives in coastal regions. However, even a 1 meter rise in sea level could submerge a few cities in Bangladesh [2]. Currently, about half the snow that falls on Greenland melts and becomes water, while the rest of it is discharged as icebergs. It is estimated that if the annual average temperature in Greenland were to rise by 3° C, this equilibrium would change, with an increase in melting outweighing the increase in snowfall [2].

To quantify what role the ice sheets will play in the rising sea level, it is essential to collect data about the net gain or loss of an ice sheet. The key parameter is the mass balance, which is the difference between the mass of snow added and the mass of snow lost. The input to the glacier is called accumulation, while the loss is called ablation. Accumulation is usually through snow, which subsequently freezes into ice. Ablation is caused by melting followed by run-off, evaporation, removal of snow by wind, and the calving of icebergs [4]. There are three methods used in determining the mass balance. The first is computing the accumulation of ice and subtracting the loss terms due to iceberg calving, surface melting, and run-off. The second is comparing the annual ice flux along the perimeter of the ice sheet to the accumulation on the ice sheet. Knowledge of ice thickness and ice velocity are necessary to compute the flux. Finally, the last major method is measurement of changes in ice volume. This is probably the most precise method, and involves the use of radar altimeters to measure changes in surface elevation [4].

Unfortunately, there are large uncertainties in the estimates of the mass balance, which make it difficult to assess what role the ice sheets play in the rising sea level [5]. As part of an effort to gain an improved understanding of the mass balance of the Greenland ice sheet, NASA started the Program for Arctic Regional Climate Assessment (PARCA). PARCA uses both spaceborne and airborne altimetry as well as ground based programs to assess the mass balance [6]. Recently, NASA launched the satellite IceSat, to monitor surface elevation with a laser altimeter to determine mass balance. The European Space Agency (ESA) will launch a satellite called CryoSat, with advanced radar altimeter for measuring surface elevation of polar ice sheets and free board of sea ice. Although these satellites will measure ice sheet growth or shrinkage, additional measurements are required to interpret observed changes. One of the key additional measurements is spatial and temporal variations in the accumulation rate.

1.2 Reasons for remote mapping of internal layers

A detailed knowledge of the accumulation rate of ice is required to estimate ice sheet mass balance and to interpret satellite measurements. The most common method of obtaining accumulation information is through the analysis of ice cores and pits [4]. As part of PARCA, extensive ice core measurements of accumulation have been made around the southern Greenland ice sheet. Over the past two decades, many point accumulation measurements have been made. These estimates are not continuous, but separated spatially and temporally. Therefore, in order to find the average net accumulation rate across a region, it is necessary to interpolate the data. However, even in the region where the most point accumulation estimates come from, the inland region above 1800 m, there is an average uncertainty in accumulation rate of 24% [7].

Figure 1.1 shows an accumulation map, which illustrates this uncertainty. The interpolation to obtain the ice-sheet wide estimate of accumulation from a collection of point measurements was accomplished through kriging. The black points show the locations of the samples, and the shading indicates how much uncertainty exists in the accumulation rate. The darker shade indicates larger uncertainty. In the areas where a large number of samples exists, the uncertainty is relatively small. Along the coastal region, where rapid thinning is occurring, there is a large uncertainty in accumulation rate. Collecting ice cores is problematic, due to the time consuming nature of ice-core sampling. Additionally, it can also be dangerous in certain areas. A better method is needed to safely obtain accumulation data to reduce the uncertainty due to sparse sampling.

Remote sensing is a method of obtaining information from a target without disturbing it. Remote sensing techniques are ideal for determining accumulation rate.
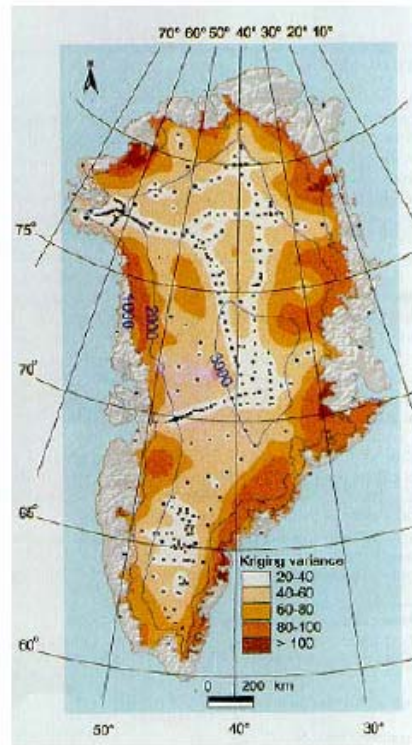
Figure 1.1: Uncertainty in Accumulation Rate [7]

The accumulation rate can be estimated by mapping a continuous profile of the dated layers in the ice sheet [8]. There are three different kinds of layers: layers due to inter-annual snowfall which subsequently refreezes, layers due to volcanic events, and layers due to melt events. Two factors enable electromagnetic detection of the layers, namely density and conductivity contrasts. Both of these factors affect the complex permittivity of a material, and electromagnetic reflections occur at boundaries of media with differing permittivity. The inter-annual and melt event layers can be detected due to density contrasts, whereas volcanic layers can be detected due to conductivity contrasts. Along with density and ice thickness information, the mapping of the shallow internal layers will allow us to estimate the accumulation rate [8].

1.3 Objectives and Approach

The objective of the thesis is to develop a compact, wideband FM-CW radar to map the near-surface internal layers with a resolution of 10 cm to a depth of 200 m. Such a high resolution requires a wide bandwidth, so the operating frequency range is from 500 to 2000 MHz. To generate this signal, we used an Yttrium Iron Garnet (YIG) oscillator in a phase-locked loop configuration. We developed a prototype, which was enclosed in a large metal enclosure. We successfully tested this radar at the North Greenland Ice Core Project (NGRIP) camp during the 2003 field season. We noted certain areas where the radar could be improved, and we incorporated these improvements in the operational radar, which fits inside one CompactPCI enclosure. This second generation radar was successfully tested at Summit Camp, Greenland, during the 2004 field season. To design both radars, we used Advanced Design System to carry out RF and Spice simulations. We used Protel DXP to lay out all of the boards.

1.4 Organization

This thesis is divided into 6 chapters. Chapter 2 presents a history of remote sensing, as well as information about reflections from internal layers, and background information on FM-CW theory. Chapter 3 provides a discussion on some of the issues considered in designing the radar. Chapter 4 discusses the actual design of the radar system. Chapter 5 discusses the experiments and results of the tests using the first- and second-generation radar systems. Finally, Chapter 6 presents some conclusions and recommendations for further work.

CHAPTER 2

Background

2.1 History of Remote Sensing of Ice

That radar could be used for ice measurements has been known since 1933, when it was discovered that snow and ice are transparent to high frequency radio signals. The ability of a Radar Echo Sounder (RES) to measure ice thickness was first demonstrated experimentally in 1957 by Amory Waite. In 1963, Evans developed the first VHF system for radio-echo sounding. This prompted several research groups and government organizations to develop RES systems. Initially, all these systems were short-pulse radar systems that operated from 30 to 600 MHz. This time-domain radar system was successful in sounding ice sheets, ice caps, and glaciers in Greenland and Antarctica [10].

The detection of internal layers was first reported by Bailey et al. in 1964 [9]. Many sources for these reflections have been discovered, including layers of liquid water, changes in the size or shape of air bubbles in the ice, and variations in ice-crystal orientation and density. Two factors mentioned in the first chapter are changes in permittivity caused by conductivity or density changes. The conductivity changes are attributable to layers of high acidity caused by violent volcanic eruptions in the past [11]. Small changes in density in the top few hundred meters cause reflections to occur from these layers [10].

In 1972, Vickers and Rose used a 1-ns pulsed radar to successfully measure snowpack thickness, density, and stratigraphy. The accuracy of the density measurements was better than 10 % [12]. In 1980, Ellerbruch and Brone [13] used an FM-CW system to correlate radar signature with density, hardness, stratigraphy, and moisture content of the snowpack. In 1982, Bogorodskiy et. al. [3], used a 1-ns pulse radar to map the internal layers in Antarctica to a depth of 5.02 m. While Bogorodskiy and others showed the feasibility of using a pulsed radar to map internal

layers, in 1990, Forster et al. [14] developed an X-band FM-CW radar to map the annual snow-accumulation layers in Antarctica with high resolution. They observed reflections up to 6 m. In 1993, researchers from the University of Munster developed a single-pulse system to measure the reflections from internal layers with high resolution [10].

Several radars recently developed at the University of Kansas show the effectiveness of using FM-CW systems to map the near-surface internal layers with high precision. In 1998, Kanagaratnam developed a 170-to-2000-MHz ground-based FM-CW radar to map the near-surface internal layers. The radar had a free space resolution of 8.2 cm and could map the layers to a maximum depth of 300 m [8]. In 2001, a 600-to-900-MHz airborne system developed by Kanagaratnam was successfully tested. In 2003, a 2-to-8-GHz radar was built to measure the thickness of snow over sea ice [15]. Table 2.1 shows a summary of the characteristics of these FM-CW radars.

Year	Operating Frequency (GHz)	Free Space Resolution (cm)	Maximum Depth (m)
1990	10-12	7.5	6
1998	.17-2	8.2	300
2001	.6-.9	50	100
2003	2-8	4	1

Table 2.1: Parameters of FM-CW Radars Developed at KU

It should be noted that a huge key in the improvement of radar systems is the advance of digital data acquisition systems, and digital signal processing [10]. Additionally, with the widespread availability of RFICs and MMICs, it is possible to build extremely compact wideband radar systems.

2.2 Reflections From Internal Layers

Reflections from internal layers are due to changes in the dielectric constant of the layer. These are caused by changes in the permittivity. The following formula shows what the reflection coefficient will be when a signal hits the interface between two media with differing permittivity constants.

$$\Gamma = \frac{\sqrt{\varepsilon_{r2}} - \sqrt{\varepsilon_{r1}}}{\sqrt{\varepsilon_{r2}} + \sqrt{\varepsilon_{r1}}} 2\sin(\frac{2\pi l}{\lambda_m}) \tag{2.1}$$

where ε_{r1} is the complex permittivity of layer 1, ε_{r2} is the complex permittivity of layer 2, l is the thickness of layer 2, and λ_m is the wavelength in layer 2. The complex permittivity depends on crystal orientation fabrics, density, impurities and temperature [16]. The three factors that influence the reflected signal in the case of near-surface internal layer mapping are density, impurities, and temperature [8].

In Greenland, there are four main zones: the dry snow zone in the center of the ice sheet, surrounded by the percolation zone, the wet snow zone, and the ablation zone. Density change usually occurs in the percolation zone due to melt events. High-density melt layers are formed when a layer of snow melts during the summer and the drainage forms a layer that later refreezes. In between the winter and summer, a new layer of snow accumulates over the melt layer. Hence the melt layer is in between two layers of low-density snow.

Variations in conductivity can also cause internal reflections. These changes are due to acidic impurities embedded in the ice due to volcanic eruptions. However, for the purposes of the experiments with this radar, we are mainly interested in detecting the layers due to density changes.

2.3 Clutter From Surface and Volume Scattering

In addition to receiving power due to reflections from the internal layers, the radar will also receive unwanted power from surface and volume scattering. Surfaces can be divided into two main classes depending on their roughness. When an

incident wave hits a perfectly smooth surface, the reflected angle will equal the incident angle, and the power of the reflected wave will depend on the dielectric contrast between the two media. This is called specular or coherent scattering. For a monostatic radar, this implies that the only way to detect reflections from a perfectly smooth surface is to observe at nadir. In the case of a rough surface, the scattering will occur in all directions, and is called incoherent scattering. If the antenna beamwidth is too large, it can detect these incoherent components even while looking at nadir, and these incoherent scattering components can mask weak coherent scattering components from subsequent layers. From calculations taken from [8], it can be shown that surface scattering will not mask the return power from the internal layers.

Volume scattering refers to scattering by small particles in an inhomogeneous medium. How much energy is scattered by these particles depends on their size relative to the wavelength of the transmit signal. The smaller the wavelength, the more energy is scattered. From calculations taken from [8], it can be seen that volume scattering has a negligible effect on the return power, and therefore can be ignored.

2.4 Calculating Return Power Using The Radar Equation

The radar equation can be used to estimate the received power given certain parameters. The following equation shows the radar equation for a perfectly flat target:

$$S = \frac{P_t \lambda^2 G^2 \Gamma^2}{(4\pi)^2 (2R)^2} \tag{2.2}$$

where P_t is the transmitted power, λ is the wavelength of the transmitted signal, G is the antenna gain, Γ is the reflection coefficient of the target, and R is the range to the target.

This equation allows us to compute the return power from internal layers. Return power will also come from surface and volume scattering, but as already mentioned, this power will not prohibit detection of the internal layers.

2.5 FM-CW Principles and Background

In an FM-CW radar, a chirp signal is transmitted for a certain duration. While it is transmitting, the echoes are received by the receiver and mixed with the transmit signal, and the result is low-pass filtered to produce a superposition of beat frequencies.
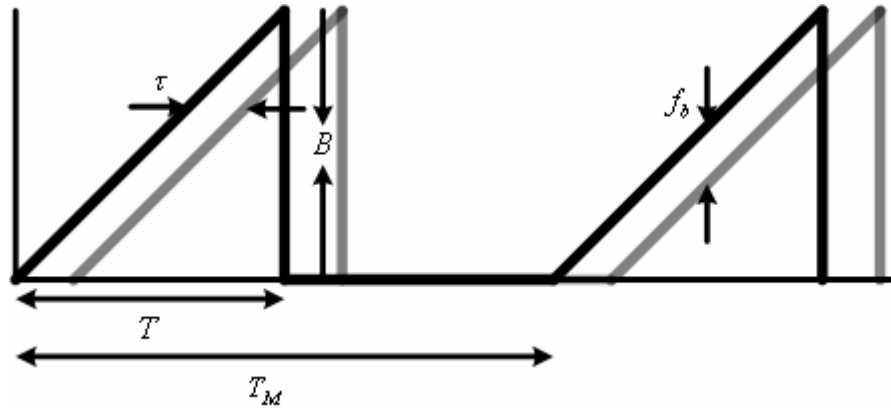
Figure 2.1: Transmit and Receive signals from a point target

The above diagram shows a transmit signal, and return from a point target. The two-way travel time is τ, the bandwidth of the transmit signal is B, the sweep time is T, and the period is T_M. At any instant in time, the transmit and receive signals are multiplied by a mixer. Since multiplying two sinusoidal signals together results in a sum and difference terms, after low pass filtering, we are left with only the difference term. The frequency of this signal is given by f_b, the beat frequency.

An expression for the beat frequency can easily be found. Using similar triangles and rearranging terms, we obtain the following expression:

$$f_b = \frac{B\tau}{T} \tag{2.3}$$

Since the beat frequency signal is time limited to T seconds, its spectrum will be a sinc function centered at $f = f_b$, and the first zero crossing will occur at $f = \frac{1}{T}$. When multiple targets exist, the result will be a superposition of many beat frequencies. In the frequency domain, two targets' beat frequencies can be as close together as $\frac{1}{T}$. Since from (2.3) we have:

$$\Delta\tau = \frac{T\Delta f_b}{B} \tag{2.4}$$

Plugging in $\Delta f_b = \frac{1}{T}$, we have $\Delta\tau = \frac{1}{B}$. Hence, the minimum resolvable separation in time between two targets is inversely proportional to the bandwidth. The two way time to a target, τ, and the range to a target, R, are related by the following formula:

$$R = \frac{c\tau}{2} \tag{2.5}$$

and the range resolution is given by:

$$\Delta R = \frac{c\Delta\tau}{2} \tag{2.6}$$

Substituting for $\Delta\tau$ in the above equation gives:

$$\Delta R = \frac{c}{2B} \tag{2.7}$$

Since the beat frequency is proportional to τ, and τ is proportional to range, knowledge of the beat frequency of any target entails knowledge of the range of that target. With many targets, we can separate them by taking the Fourier Transform of the received signal, and determine range through frequency.

We can derive an expression for the beat frequency easily. First, assume the transmit signal is given by:

$$V_t(t) = A\cos(2\pi f_0 t + \frac{\pi B}{2T}t^2 + \theta_0) \tag{2.8}$$

The signal is transmitted from the transmitting antenna, where it travels to the target. It gets reflected from any surface whose dielectric contrasts with the medium it was in. At the interface between the two media, a portion of the signal gets reflected and travels back to the receive antenna. A signal that is $\frac{\tau}{2}$ seconds away, will produce a return signal given by:

$$V_r(t) = A|\Gamma(f(t)|\cos(2\pi f_0(t-\tau) + \frac{\pi B}{2T}(t-\tau)^2 + \theta_0 + \phi(f(t))) \tag{2.9}$$

where $|\Gamma(f(t)|$ is the magnitude of the reflection coefficient at any interface, and $\phi(f(t))$ is the phase of the reflection coefficient. Both of these are a function of frequency, which varies with time.

The IF signal can be derived by mixing the received signal with the transmit signal and filtering the higher order products out. This results in the following expression for the beat frequency:

$$V_{IF}(t) = A^2|\Gamma(f(t)|\cos(2\pi f_b t + 2\pi f_0 \tau - \pi f_b \tau - \phi(f(t))) \tag{2.10}$$

2.5.1 Effects of Amplitude Modulation on IF Spectrum

Two important variations exist regarding this derivation. First, suppose the transmit signal's amplitude is not a constant. As in [17], this will result in the chirp signal being amplitude modulated, and the effect this will have on the IF signal is shown below.

Assume a signal with amplitude modulation

$$V_t(t) = (1 + mx(t))\cos(2\pi f_0 t + \frac{B}{2T}t^2 + \theta_0) \tag{2.11}$$

where $x(t)$ is any varying signal whose amplitude is no greater than 1. We have assumed that the amplitude varies around 1. A time-delayed version of this signal is given by:

$$V_r(t) = (1 + mx(t - \tau))\cos(2\pi f_0(t - \tau) + \frac{B}{2T}(t - \tau)^2 + \theta_0 + \phi(f(t))) \qquad (2.12)$$

Then, the IF signal will be given by:

$$V_{IF}(t) = (1 + mx(t) + mx(t - \tau) + m^2 x(t)x(t - \tau))\cos(2\pi f_b t + 2\pi f_0 \tau - \pi f_b \tau - \phi(f(t)))$$

$$(2.13)$$

The first term of the coefficient is normal; however, the next three represent the unwanted effects of modulation. The second and third terms will cause the spectrums of $mx(t)$ and $mx(t - \tau)$ to be modulated by the carrier, causing the characteristic AM sidebands to appear. If m is sufficiently small, we can ignore the fourth term. Thus, the effects of amplitude modulation on the spectrum will be to produce sidebands on either side of f_b. This can mask weak signals near to f_b depending on how big the sidebands are. The worst case will occur when τ is equal to 0, since the middle two terms will then add constructively. To analyze how much modulation is tolerable, we can assume that $x(t) = \cos(\omega_m t)$, since $x(t)$ can be Fourier expanded, and the effects of each term can be individually analyzed. Suppose that the ripple is given as $\pm y$ dB. The parameter m can be related to this ripple by the following equation:

$$20\log(1 + m) = y \qquad (2.14)$$

and by rearranging the equation, we see that

$$m = 10^{\frac{y}{20}} - 1 \qquad (2.15)$$

Since each sideband is down by $\frac{1}{m}$ in amplitude with respect to the carrier, if one desires that the power in the sideband be down by z dB, then we can relate z and m using the following equation:

$$z = 10\log(\frac{1}{m^2}) = 20\log(\frac{1}{10^{\frac{y}{20}} - 1}) = -20\log(10^{\frac{y}{20}} - 1)$$

<div align="right">(2.16)</div>

Figure 2.2 shows a graph of the effect of amplitude variation on the first sideband level
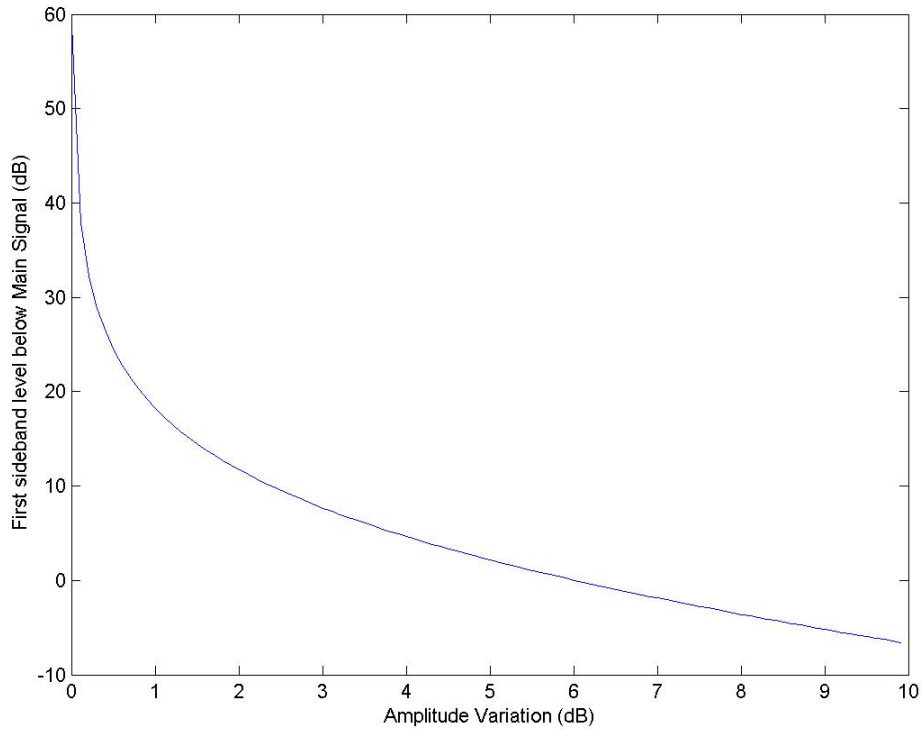
Figure 2.2: Sideband Power Level Below Main Signal vs. Variation in Amplitude of Transmit Signal

This could be a problem when detecting internal layers if the return from one layer is far below the return from an adjacent layer. This could happen if there is a large density contrast between two layers and a very small density contrast between the next pair of layers.

2.5.2 Effects of Frequency Modulation on Received Spectrum

The next case is the case of frequency/phase modulation. In this case, the phase of the chirp signal is not perfectly quadratic, but has an error term, $\Delta\phi(t)$, added to it. Again, ignoring the amplitude, the transmit signal can be expressed as:

$$V_t(t) = \cos(2\pi f_0 t + \frac{\pi B}{2T}t^2 + \theta_0 + \Delta\phi(t)) \tag{2.17}$$

and the received signal, $\frac{\tau}{2}$ seconds away, can be expressed as:

$$V_r(t) = \cos(2\pi f_0(t-\tau) + \frac{\pi B}{2T}(t-\tau)^2 + \theta_0 + \phi(f(t)) + \Delta\phi(t-\tau)) \tag{2.18}$$

The beat frequency can be derived by multiplying the transmit and receive signals, and eliminating the high frequency terms. This produces the following expression:

$$V_{IF}(t) = \cos(2\pi f_b t + 2\pi f_0 \tau - \pi f_b \tau - \phi(f(t)) + \Delta\phi(t) - \Delta\phi(t-\tau)) \tag{2.19}$$

Assuming the phase distortion term is linear over the time interval τ, and ignoring the constant phase term $2\pi f_0 \tau - \pi f_b \tau$ and $\phi(f(t))$, we can write this function as [17]:

$$V_{IF}(t) = \cos(2\pi f_b t + \tau\frac{d}{dt}\Delta\phi) \tag{2.19}$$

There are two cases we can consider, one where the oscillator is unlocked, and one where it is locked. In the case of an unlocked oscillator, a first-order model would consider the noise causing the phase variation to be Gaussian white noise, and we can represent it as a sum of sinusoids with random phase and constant amplitude. This kind of model is useful when the phase variations are short term, because we can use the narrowband FM approximation when writing the signal's spectrum. If there is slower variation or long-term instabilities, which cause the oscillator's frequency to fluctuate a lot, then this model is not very useful, since the narrowband approximation

no longer applies. Since the transmit signal is generated by a voltage (or current) controlled oscillator, we can use frequency modulation analysis to analyze the phase variation. If we let the noise be a sum of sinusoids spaced at 1 Hz intervals, using the relationship between phase and frequency, we can write $\Delta\phi(t)$ as:

$$\Delta\phi(t) = \sum_i 2\pi f_\Delta \sqrt{2}e_n \int_o^T \cos(\omega_i t + \phi_i)dt$$

(2.20)

where e_n is the rms value of the noise voltage. f_Δ is the frequency sensitivity of the oscillator. In addition to occurring in time, the phase variation also occurs over the swept bandwidth. If we call f_i the period of one cycle as a function of frequency, then we can write ω_i as:

$$\omega_i = \frac{2\pi}{f_i} \cdot \frac{B}{T}$$

(2.21)

Taking the derivative of this sum and plugging it into the above equation gives:

$$V_{IF} = \cos(2\pi f_b t - \tau 2\pi f_\Delta \sqrt{2}e_n(f)\sum\cos(\omega_i t + \phi_i))$$
(2.22)

This is recognizable as narrowband FM, where $\beta = \tau 2\pi f_\Delta \sqrt{2}e_n$ and is much less than 1. Interestingly, in contrast to amplitude modulation, having a short delay reduces the effect of frequency modulation. The spectrum of the signal can be seen by using the following narrowband FM approximation:

$$\exp(j\omega_b t)\left[1 + \sum \frac{\beta}{2}\exp(-j\omega_i t) - \frac{\beta}{2}\exp(j\omega_i t)\right]$$
(2.23)

So, the result on the beat frequency spectrum is to produce sidelobes at $\pm\omega_i$, whose amplitude is $\tau\pi f_\Delta \sqrt{2}e_n$. This allows us to place a constraint on e_n depending on how far down we want these sidebands. If the furthest we wish to map is 200 m,

then τ will be 2 μs. Also, as will be discussed later, f_Δ in our case is 3.33×10^9 Hz/V. If one desires that the power in a sideband be down by z dB, then we can relate z and e_n through equation 2.24.

$$z = \frac{1}{10\log(\dfrac{1}{(\tau\pi f_\Delta \sqrt{2}e_n)^2})} = \frac{1}{-20\log(\tau\pi f_\Delta \sqrt{2}e_n)}$$ (2.24)

Using the values above for τ and f_Δ, we can graph z and e_n, as shown in Figure 2.3.
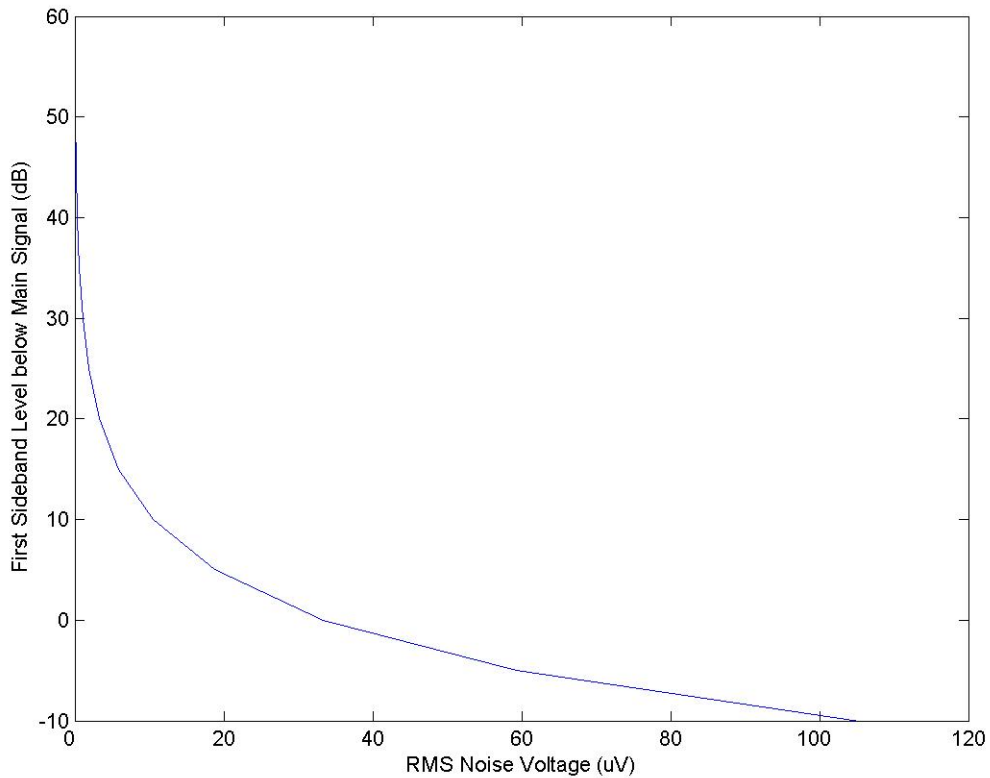
Figure 2.3: Sideband Power Level Below Main Signal vs. RMS Noise Voltage

This analysis is valid for an unlocked oscillator, whose phase noise can be modeled using the narrowband FM approximation. However, in our case, we will be using a locked oscillator. A locked oscillator will also have phase noise, but its characteristics will be different. The noise inside the loop bandwidth will be a combination of two terms, the first one being an rms combination of the reference noise plus the divider noise both multiplied by the forward gain of the loop divided by the loop gain plus one [22]. Symbolically, this is written as:

$$(S_{REF}{}^2 + S_N{}^2)(\frac{G}{1+GH})$$

(2.25)

This will be added to the noise from the charge pump of the PLL (the PLL topology will be explained in Section 3.2.2), which can be written as:

$$S_{CP}{}^2(\frac{1}{K_D})^2(\frac{G}{1+GH})^2$$

(2.26)

Outside the loop bandwidth, the noise will follow the noise of the VCO, which can be written as:

$$S_{VCO}{}^2(\frac{1}{1+GH})^2$$

(2.27)

The function $(\frac{1}{1+GH})^2$ is a high pass filter, and so at frequencies well outside the loop bandwidth, it will pass all the VCO noise.

Theoretically, we could construct a noise model by finding the functions G and H, and adding these terms in an rms fashion. However, as the loop filter order is increased, it is difficult to do this analytically. It could be done by simulation, but since we have already developed a model for the unlocked VCO that approximates the phase noise of the locked VCO outside the loop bandwidth, we will use this model. Of course, this model should overestimate the noise contribution inside the bandwidth, but it will give us a rough estimation of what kind of problem the noise will be.

2.6: Prism Project Objectives

This radar was built as part of the Polar Radars for Ice Sheet Measurements Project (PRISM). Sponsored by NASA and NSF, PRISM was undertaken at the University of Kansas in 2001 with the goals of measuring including accumulation rate and ice thickness, depth and shape of internal layers, subglacial topography, and basal conditions. To achieve this, a multi-disciplinary team is developing a sensor web for ice sheet measurements. The initial web consists of two autonomous rovers, which contain the radars for ice sheet measurements as well as sensors for navigation, hazard detection, and communications. The three radars are:

1. A synthetic aperture radar (SAR), which can be operated in monostatic or bistatic mode, and is capable of generating two-dimensional reflectivity maps of the bed to determine basal conditions.

2. A wideband depth sounding radar for measuring ice thickness and deep internal layers.

3. A wideband accumulation radar for mapping the near-surface internal layers.

During the first two years of the project, prototypes of the depth sounder, accumulation radars and rovers were developed, and they were tested at the NGRIP camp in Greenland during the 2003 field season. We redesigned and developed optimized systems that can be housed in CompactPCI chassis. Both the depth sounder and accumulation radars were tested in at Summit, Greenland during July, 2004. Additionally, a prototype of the SAR radar was tested using the rover.

CHAPTER 3

Design Considerations

3.1 Introduction

When designing a surface-based radar system, both electrical and mechanical considerations are important. A surface-based system should be lightweight and compact, and the parts of the system should be easily interchangeable. With this in mind, we developed an extremely compact wideband FM-CW radar, which fits in one CompactPCI chassis. We stated earlier that we desire a resolution of 10 cm in free space. This is a major reason for choosing an FM-CW radar system over a pulsed radar system. In the case of a pulse-compression radar system, we must sample the received signal at least twice the highest frequency. In our case, this would be 4 GHz. Digitizers which sample this fast would be very expensive and large, defeating the goal of making the radar compact and lightweight. The same is true for a simple pulse radar. In order to get a 10-cm resolution, we would need to have a pulse of .66 ns. Generating and digitizing such a narrow pulse would be difficult to achieve. Additionally, we want to map the near-surface internal layers to a depth of about 200

m. If we use a pulse compression radar, there is no easy way to get the dynamic range required to see both the top layers and the bottom layers. The reflection from the top layer is so strong, so we would need to gate it out to avoid saturating the receive components. In this case, we wouldn't be able to see the top layers. On the other hand, if we attenuated the signal from the top layers, we may not be able to see the weaker returns from the bottom layers. In an FM-CW radar, we bypass this problem by using a high-pass filter in the receiver which knocks down the power from the top layers, but still enables their detection.

3.2 System Description

The block diagram of the radar is shown in Figure 3.1. This radar consists of 5 modules. The first module is the signal generation board, which uses a phase-locked loop to achieve a highly linear sweep from a YIG oscillator

The next section is the Automatic Gain Control circuitry, to level the power before transmitting, since we have seen that the effects of ripple in the transmit signal cause unwanted sidelobes to appear in the IF signal spectrum. We use a phase-locked oscillator (PLO) section to down-convert the YIG output from 4.5-to-6 GHz to 500-to-2000 MHz. The PLO's output frequency is 4 GHz. Also in this module is a PLO whose frequency is 50 MHz. The purpose of this is to supply the Data Acquisition system with a clock.

The front end of the receiver consists of a filter, amplifier, and mixer. The purpose of this section is to simply down-convert the received signal for the IF stage. The IF stage consists of a high-pass filter to reduce the antenna feed-through, an op-amp to provide any necessary gain, and a low-pass filter, to cut off any unwanted high frequency signal or noise.

3.2.1 System Specifications

In order to calculate how many integrations we can perform, we must first calculate the correlation length. For an unfocused airborne SAR, the correlation length is given by the formula below:

$$L_{MAX} = .5\sqrt{R\lambda} \tag{3.1}$$

Since the highest frequency will have the lowest wavelength, we will calculate the length for the highest frequency, which is 2 GHz. R is the height of the antennas above the ground, which in our case will be approximately 2.5 m. Plugging these values in, we find that L_{MAX} = .306 m. Using the Equation 3.2, we can calculate how many coherent integrations can be performed.
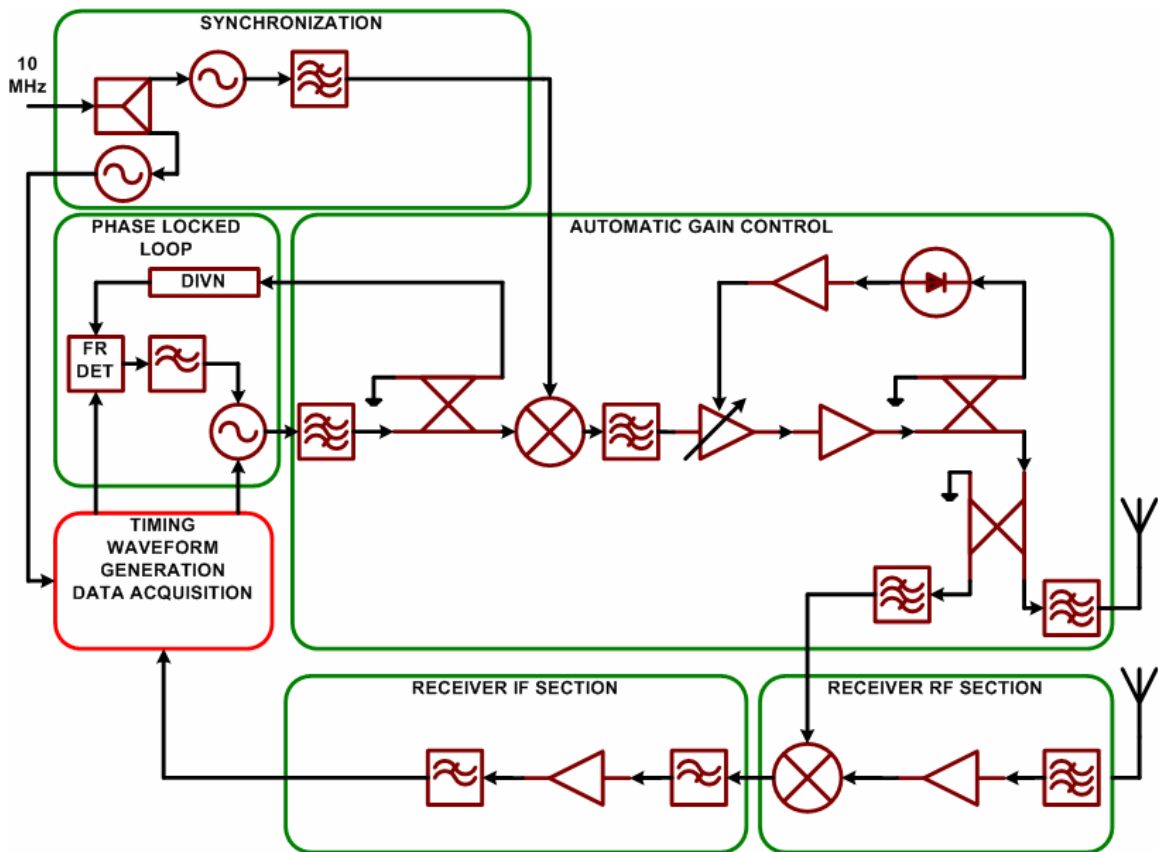
Figure 3.1: Block Diagram of Accumulation Radar System

$$\frac{PRF \cdot L_{MAX}}{v} \geq N \tag{3.2}$$

where PRF is the Pulse Repetition Frequency and v is the velocity of the vehicle. We are limited to a PRF 180 Hz, and a velocity of 2.78 m/s. Therefore, at 2 GHz, we are limited to 20 coherent integrations. At 500 MHz, we can perform twice as many, or 40 coherent integrations.

To decide how much transmit power and receiver gain is needed, we must first determine the noise figure of the receiver, A/D dynamic range, and expected return power.

We are using a 12-bit A/D converter, which can digitize signals from -.5 to .5 V. The maximum signal to noise ratio of a converter is given by the following formula:

$$SNR = \frac{3Q^2}{2}$$

(3.3)

where Q is the number of quantization levels, which is 2^N, for an N bit digitizer. For a 12-bit digitizer, this corresponds to 74 dB SNR. The power of the maximum signal that can be digitized in a 50 Ω system is:

$$P_{MAX} = \frac{V_p^{\;2}}{2R} = \frac{.25}{100} = 2.5\,mW = 4\,dBm \tag{3.4}$$

Since the maximum signal to noise ratio is 74 dB, the A/D noise floor is -70 dBm.

The noise floor of the radar system is given by:

$$N = kTBF \tag{3.5}$$

where k is the Boltzmann's constant (1.38×10^{-23} J/K), T is the ambient temperature (290 K), B is the bandwidth of one range bin, and F is the noise figure of the receiver. The bandwidth of the range bin is the sampling rate divided by the number of DFT points before zero padding. Since we are sampling at 10 MHz, and

sweeping over 4 ms, the number of DFT points is 40,000 points, and the bandwidth is 250 Hz.

The noise figure is given by the Friis formula:

$$F = F_1 + \frac{F_2 - 1}{G_1} + \frac{F_3 - 1}{G_1 G_2} + \dots \frac{F_N - 1}{\prod_{n=1}^{N-1} G_n}$$

(3.6)

The front end of the receiver consists of a bandpass filter, a 3 dB attenuator, amplifier, and another 3 dB attenuator. The characteristics of these components are given in Table 3.1.

Stage N	Component	Gain (dB)	Noise Figure (dB)
1	Filter	-.5	.5
2	Attenuator	-3	3
3	Amplifier	26.5	5.5
4	Attenuator	-3	3

Table 3.1: Characteristics of Receiver Front End Components

Using the formula above, the noise figure is $\approx$ 9 dB. Plugging this into the formula for minimum detectable signal, we get that:

$$MDS = -140 \; dBm$$

(3.7)

The radar equation can be rewritten by taking the logarithm of both sides of equation 2.2. This results in:

$$S = P_t + 2\lambda + 2G + 10\log_{10}|\Gamma|^2 - 20\log_{10}(4\pi) - 20\log_{10}(2R)$$

(3.8)

In order to get a better idea of what the reflected power is, we can include the effects of losses due to scattering and absorption. The two-way loss through a media due to the extinction coefficient is given by:

$$\alpha = \exp(-2R\kappa_e) \qquad (3.9)$$

Plugging this into the above equation, the total return power is:

$$S = P_t + 2\lambda + 2G + 10\log_{10}|\Gamma|^2 - 20\log_{10}(4\pi) - 20\log_{10}(2R) - 20R\kappa_e \log_{10}(\exp(1))$$

$$(3.10)$$

We can compute the loss due to scattering and absorption as a function of frequency. Furthermore, since we want to see up to 200 m in ice, we need the power reflection coefficient at this depth. We had ice core data up to a depth of 150 m. Using a simulation package, we simulated what the expected power reflection coefficient would be at a depth of around 150 m [23]. This value turned out to be basically independent of frequency, and is approximately –43 dB. It can be shown that the absorption loss dominates at the frequencies we are interested in, and the values for absorption loss at our frequency at a depth of 150 m can be found in [8]. Assuming a transmit power of 0 dBm, and plugging these numbers in the above equation using R = 150 m, Table 3.2 shows the return power at a few frequencies:

Frequency (MHz)	Lambda (cm/dB)	Gain (dB)	PRC (dB) 150 m	S (dB)
500	60/-2.2	7.5	-43	-108
1000	30/-5.2	7.0	-43	-117
1500	20/-7.0	8.4	-43	-121
2000	15/-8.2	3.0	-43	-138

Table 3.2: Expected Return Power from Layer at a Depth of 150 m

This calculation shows that at 2 GHz, the signal will barely be above the noise floor. We decided to transmit around 20 dBm, which is more than enough to enable detection at 150 m.

To compute how much gain the receiver should have, we assume that a 10 dB signal to noise ratio is required above the A/D converter noise floor. In terms of an equation, we desire that

$$P_T + S + IntGain + G_{RCR} > A/D\,Noise\,Floor + SNR \tag{3.11}$$

We will assume that 10 coherent integrations are performed, so, rearranging the equation to find the gain, we find that $G > 44$.

In the receiver, there is about 23 dB of loss. The front-end amplifier has a gain of 26 dB, and the IF amplifier has a gain of around 55 dB, making the total gain 58 dB. We used this much gain in case there were any errors in our calculations. Also, this much gain will enable us to detect layers well beyond 150 m. Finally, if this gain is not required, it is relatively simple to lower the gain of the IF amplifier.

In Chapter 2 we looked at the effects of amplitude and frequency modulation on the beat frequency spectrum. In order to quantify how much variation is tolerable, we looked at the return power from a sample core to a depth of 150 m, using the same simulation package as above. This simulation package ignores spreading, scattering and absorption loss, but we are only interested in the difference in return power between layers near to one another. These data are from the dry snow zone, which is where we will be operating this radar. The layers are spaced approximately 1 m apart. From the plot of the return power, we found that the maximum difference in power between two layers next to one another was about 20 dB. So as long as the sidebands due to amplitude and frequency modulation are more than 20 dB down, this should not limit detection of internal layers.

Table 3.3 summarizes the important system parameters.

Frequency (MHz)	500 to 2000
Sweep Time (ms)	4 ms
Transmit Power (dBm)	20
Antenna Type	TEM Horn
A/D Dynamic Range	12-bit 72 dB

Table 3.3 System Parameters

3.2.2 Phase-Locked Loop System Overview

The purpose of the phase-locked loop section is to phase-lock the swept 4.5-to-6-GHz chirp signal to a stable, low-frequency source. Though we desire a 500-to-2000-MHz transmit signal, finding a YIG that could tune this bandwidth quickly was very difficult. For airborne applications, it is necessary to sweep quickly, and we designed the PLL section with an airborne application in mind. Also, an oscillator in this bandwidth would have 2nd order harmonics up to 1000 MHz in band. Therefore, we decided to use a fast YIG oscillator that could tune between 2-to-8-GHz, sweep it from 4.5-to-6-GHz, and mix it down to 500- to-2000-MHz. YIG stands for Yttrium Iron Garnets, which is a small sphere that resonates at a particular frequency when a magnetic field is applied. Since the YIG is lossy, a circuit is needed to replace the lost energy. Since any resonator can be modeled as a parallel RLC circuit, a negative resistance in parallel with this will cancel the lossy resistance. This is typically achieved by using an FET or transistor [24]. As stated above, in order to get the sphere to resonate, a magnetic field is needed. An inductor is used to couple energy to the sphere. Since current through an inductor will produce a magnetic field, a high quality current source can be used to tune the YIG. There is also a small resistance in series with the inductor, and together this constitutes the main coil of the YIG. The main coil typically has a bandwidth in the low kHz range, so it cannot be swept very fast. In addition, YIG's have an alternate coil, the FM coil, which can be used to either frequency modulate or phase lock the oscillator. Since the FM coil has a much smaller inductance and resistance, the FM coil has a much higher tuning bandwidth than the main coil, on the order of 1 to 2 MHz. YIG's have excellent linearity, which can be as low as $\pm$ .1% deviation from perfect linearity.

Previously, the snow radar had used a YIG oscillator whose main coil was phase locked. This has the advantage of ensuring that the phase of the signal from the YIG is locked to the phase of a stable low-frequency reference source. However, the

sweep speed is limited by the main coil bandwidth, which, as stated before, is relatively small. Therefore, in order to achieve both a phase-locked and fast sweep, the FM coil can be used to correct the non-linearity of the main coil on the "fly," since its bandwidth is a lot larger than the main coil's.

Broadly speaking, this system consists of a Phase-Locked Loop (PLL) chip (the LMX2326 from National), a YIG oscillator, and a Divide-by-8 chip (Hittite HMC363G8). The PLL consists of a Divide-by-N, Divide-by-R, and a phase/frequency detector with a charge pump. The goal of this system is to apply a ramp voltage to the YIG's main coil, which will produce a corresponding chirp signal from the YIG. This chirp signal is then fed back through a coupler to the Divide-By-8 chip. This is necessary because the LMX2326 cannot handle frequencies above 1.8 GHz.

Since the YIG output is 4.5-to-6-GHz, it must be divided down before going into the PLL. Once inside the PLL, it is again divided by N, and compared with the stable, low frequency chirp at the Phase/Frequency detector generated by the digital system. Any difference in phase between the two is then filtered and drives the FM coil.
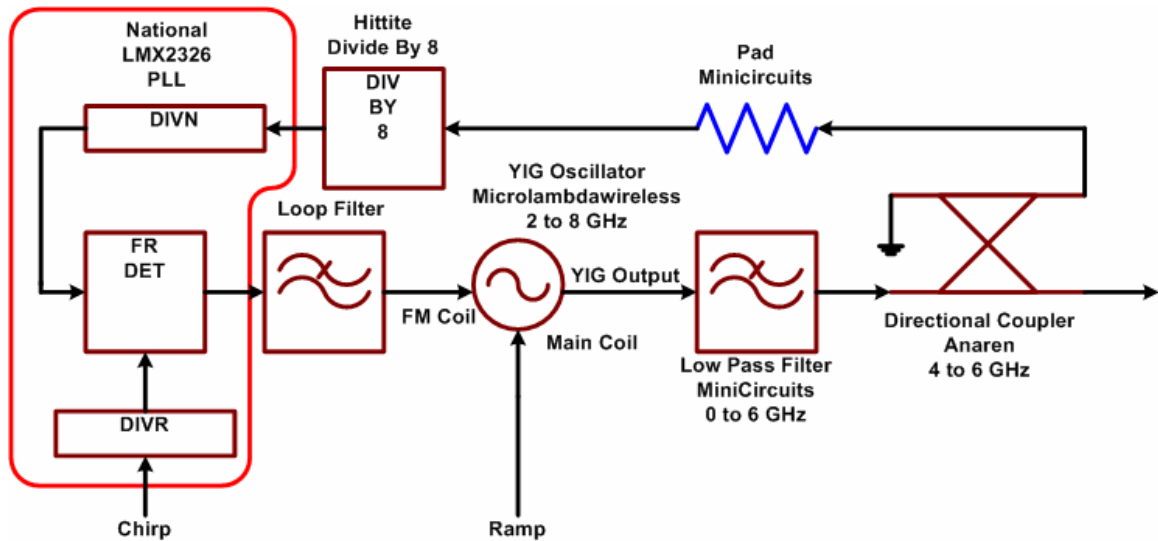
Figure 3.2 : Block Diagram of Phase-locked Loop section

Figure 3.3 shows the block diagram of the LMX2326 from National. The OSC_{IN} block is where the low-frequency, stable chirp comes in. It is buffered and converted into a digital signal, before going into the 14-bit R counter, which serves as a divider, to divide it down to a reasonable comparison frequency. At the same time, the YIG signal, divided by 8, is F_{IN}. This signal is also buffered in the prescaler block, which serves as a divider. In addition, there is an 18-bit N counter which also serves as a divider. This gives the option of fractional division.

After being divided to the same comparison frequency, the two chirp signals go into the phase comparator, which drives the charge pump. The purpose of these blocks is to determine whether the two signals are aligned in phase or not. In addition, there is a lock detect pin, which indicates whether the YIG signal is locked to the reference.

Figure 3.4 shows how the phase detector/charge pump works. The charge pump consists of two matched P and NMOS transistors. The PMOS is tied to the charge pump power supply, while the NMOS is tied to ground. On the top, we have the reference signal divided by R. The middle is the feedback output from the

oscillator, divided by N. When the reference signal's rising edge occurs before the fed-back signal's rising edge, the output from the charge pump sources current until it sees the rising edge of the fed-back signal. On the other hand, if the rising edge of the fed-back signal occurs first, the charge pump sinks current, until it sees the rising edge of the reference. When both signals are perfectly in phase, the charge pump will "shut off," or go into tri-state, where it will, in theory, neither source nor sink current.
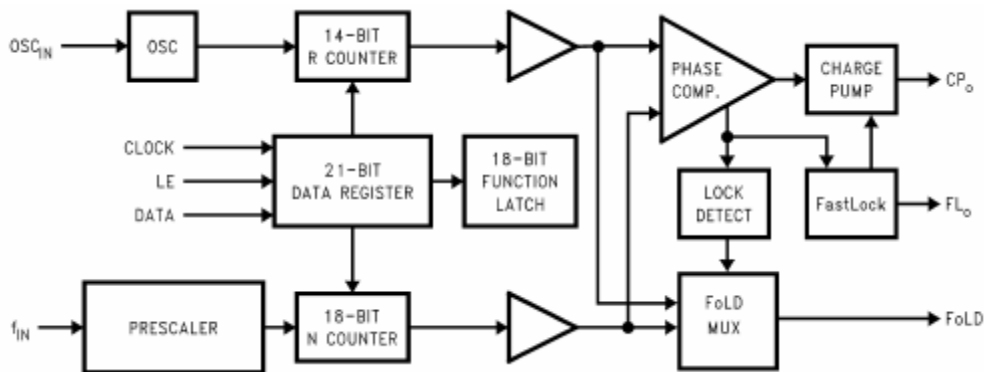
Figure 3.3: LMX2326 Block Diagram

The output from the charge pump will be filtered by the loop filter, and fed into the FM coil driver, which takes a voltage and converts it into a tuning current. Similarly, the main coil also has a driver, which takes the applied ramp voltage signal, and converts it into a current, which produces the 4.5-to-6-GHz chirp. Thus, the goal of this system is, through the use of feed back, to use the FM coil to correct any non-linearity in the spectrum produced by the YIG's main coil.
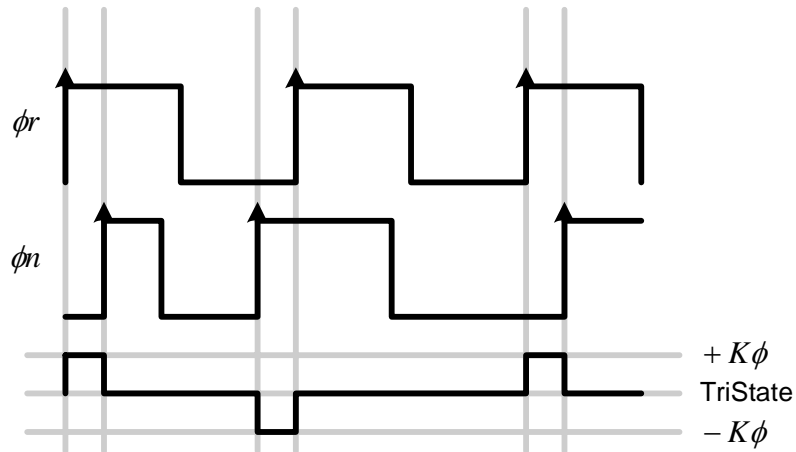
Figure 3.4: How the Charge Pump Works

Also included in this board is the Divide-by-8 chip from Hittite. This is a GaAs chip, which operates up to 12 GHz. Detailed analysis of the circuits in the system will be presented in the next chapter.

3.2.3 Automatic Gain Control System Overview

The next phase of the transmitter is the Automatic Gain Control (AGC) circuit. The purpose of the AGC is to level the transmitter power. We have already seen what effect amplitude modulation has on the beat frequency return. Therefore, it is important to determine what kind of variation is tolerable. From Figure 2.2, if a sinusoid with 2-dB peak-to-peak variation modulates the transmitted waveform, this will result in the sidebands being down by 20 dB. Typically, the modulation will be low frequency, which would result in sidebands close to the carrier. If the return from a layer is very weak, then these sidebands could mask it.

Figure 3.5 shows the diagram of the AGC circuit. After the YIG signal gets mixed down and filtered, it is passed to a Variable Gain Amplifier (VGA). A control voltage to the VGA determines the gain of the VGA. After the VGA, the signal goes through an amplification section, which boosts the signal power to the required level for transmitting. The signal is then fed to a coupler, and the coupled signal is fed into

an RF detector, which produces a voltage proportional to the input power. This voltage is then conditioned and filtered by low-frequency feedback circuitry, and the filtered signal is used to control the gain of the VGA. The rest of the signal is fed to another coupler, and part of the signal is coupled into the mixer of the receiver, while the rest is transmitted by the transmit antenna.
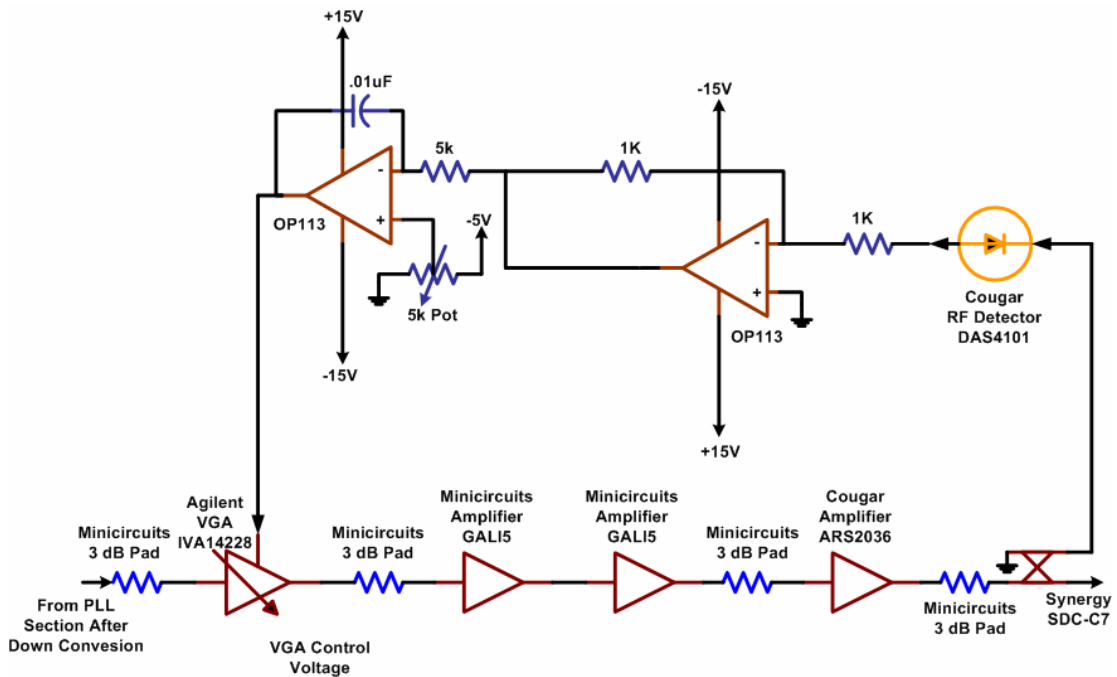
Figure 3.5: Automatic Gain Control System

3.2.4 Phase-Locked Oscillator System Overview

The purpose of the Phase-Locked-Oscillator (PLO) system is to provide a low-noise, stable 4 GHz LO to down convert the signal from the YIG from 4.5-to-6-GHz to .5-to-2-GHz. Additionally, the Data Acquisition system requires two 50-MHz clocks to operate. The PLO board receives a 10 MHz signal from a Rubidium source as a reference signal. We purchased two PLOs from Synergy that accept 10 MHz and produce 4 GHz and 50 MHz, respectively. We amplified and filtered the 4 GHz signal before passing it to the LO port of the mixer. We split the 50 MHz signal

in two and fed these signals through the front panel to the digital system. Figure 3.6 shows the block diagram of the PLO system.
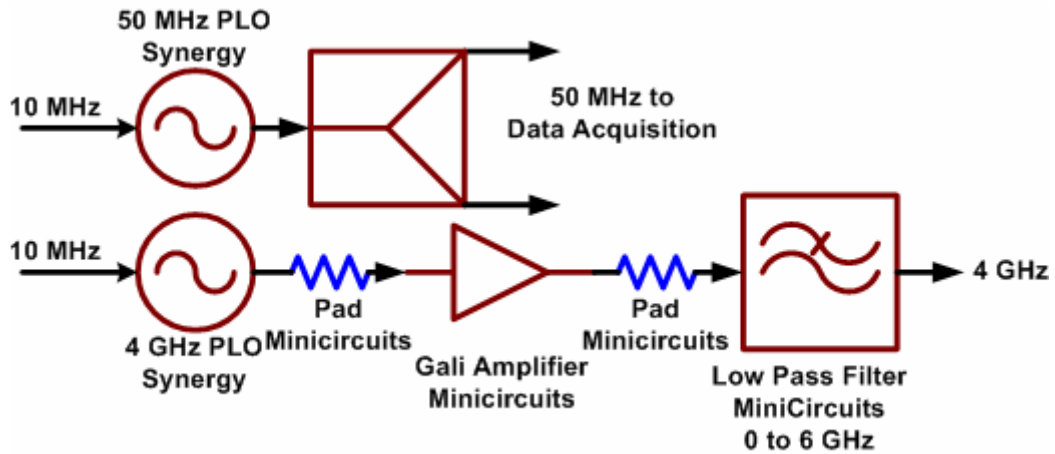
Figure 3.6: Phase-Locked Oscillator System

3.2.5 RF Section Overview

The next stage is the front end of the receiver, which is the RF stage. This section amplifies the return signal and passes it to a mixer, whose LO is the transmit signal. The block diagram of the RF stage is shown in Figure 3.7.

The high reverse isolation amplifier is necessary to prevent the signal from leaking back to the receive antenna and being transmitted. The main consideration in this stage is making sure that the power going into the RF port of the mixer is at least 15 to 20 dB below the power going into the LO port of the mixer. This can become a problem because the power received from the top layers will be relatively large. The larger the difference between the LO and RF power, the less of a problem third-order products will be. Third-order products and spurious signals in general are unwanted because they can mask layers or be mistaken as layers themselves.
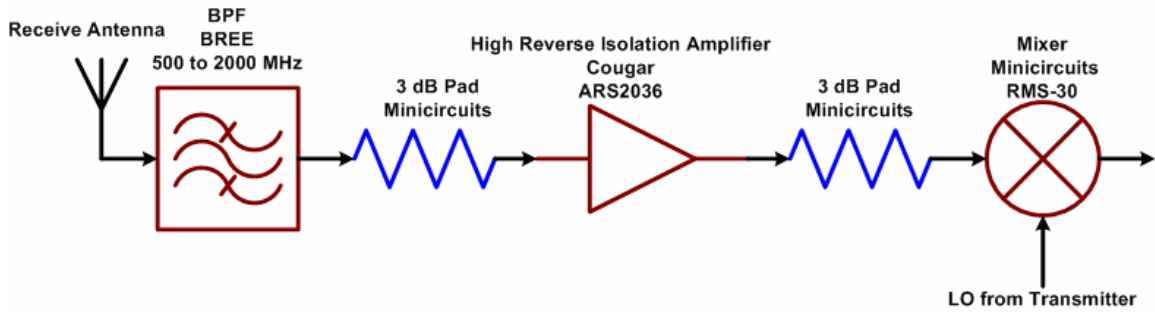
Figure 3.7: Block Diagram of RF System of the Receiver

3.2.6 IF Section Overview

The final section of the receiver is the IF section, which amplifies the signal so that it can be digitized and captured by the Data Acquisition system. The antenna feed-through presents a problem for the IF amplifier and A/D converter, since they can become saturated. To circumvent this problem, a high-pass filter, whose cutoff frequency is above the antenna feed through frequency, is necessary. An ordinary filter won't do, since it known that an ordinary filter can result in large settling time, ringing, and saturation of the IF amplifiers [8]. Therefore, we used a Gaussian high-pass filter. The advantages of a Gaussian filter are fast settling time and little ringing. To design this filter, we need to know at what frequency the feed-through signal comes. This calculation is shown in the following chapter. We also need to know what the beat frequency will be due to the echo from layers at around 200 m. This will tell us what kind of op-amp we need, and what the cutoff frequency of the low-pass filter should be before the signal gets digitized. Figure 3.8 shows a diagram of the IF stage, which will be discussed in more detail in the following chapter.
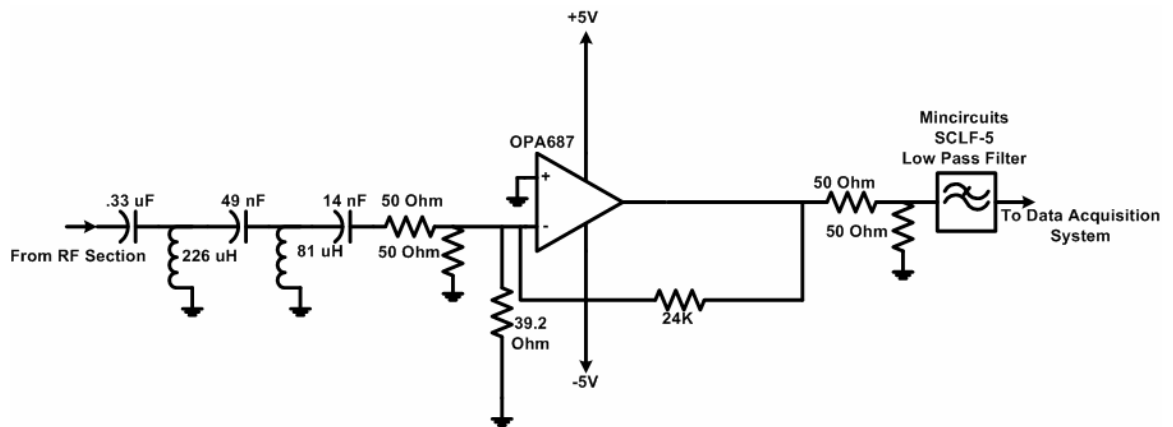
Figure 3.8: Diagram of IF Section of the Receiver

CHAPTER 4

SYSTEM DESIGN

4.1 YIG System-Main Coil Driver Circuit

The first step in designing the PLL circuit was the design of a main coil driver. As stated in Chapter 3, the purpose of the main coil driver is to take a voltage and convert it into a current that can drive the YIG oscillator. The YIG we are using is the 2-to-8-GHz oscillator MLMH0208 from Microlambdawireless. Table 4.1 shows some pertinent specifications of the oscillator and the main coil.

First, we see that the main coil sensitivity is 10 MHz/mA, which means that it takes 200 mA through the main coil to produce 2 GHz, and 450 to 600 mA to produce a chirp from 4.5 to 6 GHz. In order to drive this much current, a current amplifier is needed. A high-power BJT can perform this function. In addition, some way of getting a constant current to flow through the main coil in the absence of any input signal is needed. This would be the YIG's free running frequency. For this, a Zener reference source can be used, and summed with the input signal in an op-amp summer to produce the total signal.

Figure 4.1 shows the first main coil driver design used. All the resistor values were calculated using the formulas below. We will backwards justify them. The purpose of the first op-amp is to buffer the input signal from the rest of the circuit, and to provide any necessary gain. The voltage ramp provided from the waveform generation card can provide any voltage between –1 and 1 V, but we decided to sweep it from 0 to .5 V initially, as this was convenient. The first op-amp had a gain of –20, and thus the voltage at the output of the first op-amp was between 0 to –10 V. When the voltage is 0 V, this corresponds to the free running oscillator condition.

The second op-amps negative terminal will be forced to 0 V due to feedback, and so the current through the 26 kΩ resistor will be 0. The current through the 4.99 kΩ resistor will always be

$$I_{4.99k\Omega} = \frac{V_{out}}{4.99K} \tag{4.1}$$

Since the zener diode will produce -6.2 V in the configuration below, the current through the 56 kΩ resistor is given by:

$$I_{56K} = \frac{6.2}{56K} = 110\mu A \tag{4.2}$$

This is a constant current through this resistor. In the case when there is no input voltage, this same current flows through the 4.99 kΩ resistor as well. Equating the two expressions above, and solving for V_{OUT} gives approximately .6 V .6 V across a 3 Ω resistor produces 200 mA through the 3 Ω.

Frequency Range	2 to 8 GHz
Power Output min.	+13 dBm
Power Output Variation max.	+/- 2 dB
2nd Harmonic, min.	-12 dBc
3rd Harmonic, min.	-20 dBc
Spurious Output min.	-70 dBc
Phase Noise @ 10 KHz	-98 dBc
Main Coil	
Sensitivity	10 MHz/mA
3 dB Bandwidth	25 kHz
Linearity	+/- .25%
Input Impedace @1kHz	4 mH and 4 ohm

Table 4.1 YIG Characteristics

Since the op-amp cannot supply this kind of current alone, the BJT is necessary, and amplifies the current in its base. This same 200 mA flows through the main coil, which produces the 2 GHz free running signal. The first op-amp inverts

and multiplies the input signal by 20. Therefore, the voltage at the output of the first op-amp is $-20V_{IN}$. Since V_{IN} ranges from 0 to .5 V, the most negative voltage at the output is -10 V.
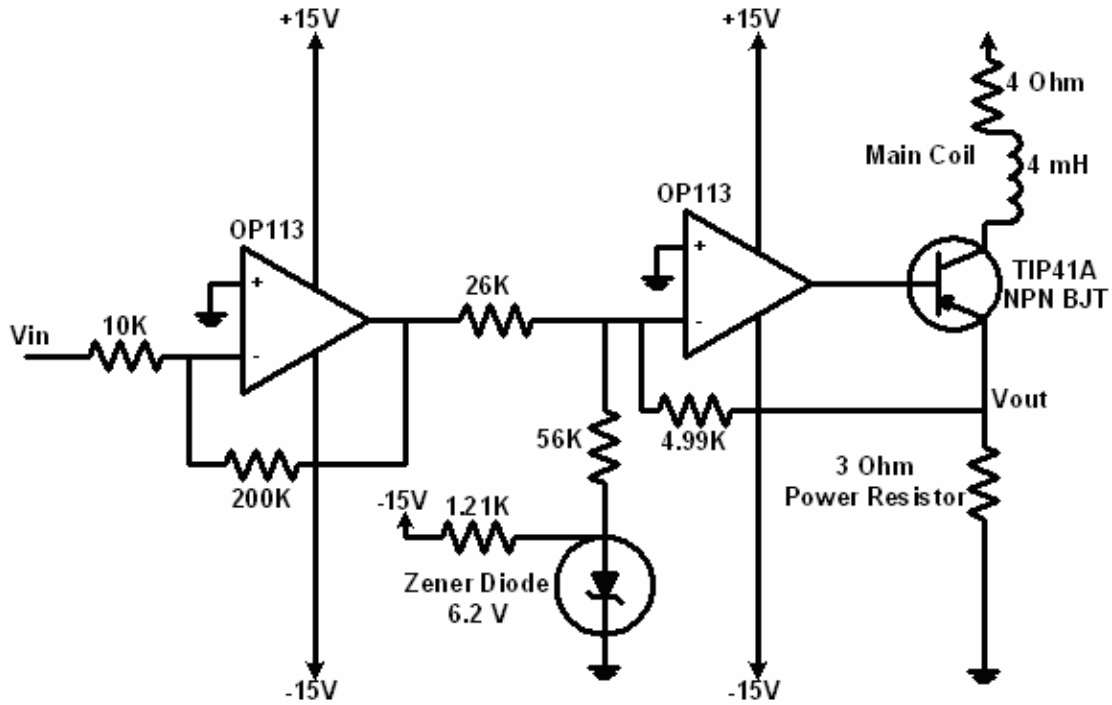
Figure 4.1: Main Coil Driver Circuit

When the voltage is -10 V, the current through the 26 kΩ resistor is:

$$I_{26K} = \frac{10}{26K} = 385 \ \mu A \tag{4.3}$$

We already calculated the current through the 56 kΩ to be 110 μA, so the total current flowing through the 4.99 kΩ is $110 + 385 = 495$ μA. The voltage at V_{OUT} will be approximately 2.5 V, which will produce a current of about 833 mA through the 3 Ω resistor and hence through the main coil. This will give an output frequency of approximately 8 GHz, which is desired. Therefore, with an input voltage of 0 to .5 V, we can get any frequency between 2 to 8 GHz. By adjusting the input voltage, we can obtain a sweep of 4.5-to-6 GHz.

There are some problems with this configuration, however. The first is that of noise. Because the main coil's sensitivity is 10 MHz/mA, to get 10 MHz deviation we need just 1 mA of noise. To get 1 mA of noise, we just need 3 mV of noise across the 3 Ω resistor. Since the first op-amp has a gain of 20, this will greatly amplify the noise of the first op-amp. We can reduce the noise significantly by designing a driver that tunes only from 4.5 to 6 GHz, and extending the input ramp voltage from -1 to 1 V. Also, having some kind of a filter to reduce the bandwidth of the circuit would be beneficial, since currently, the bandwidth is only limited by the coil's bandwidth, which is 25 kHz. This much bandwidth is unnecessary for the speeds at which we are sweeping. The next problem is that the second op-amp oscillates. In order to stop it from oscillating, compensation is required. This will have the benefit of reducing the bandwidth as well, which helps mitigate the noise problem. Figure 4.2 shows a simulation of the main coil current when the op-amp is uncompensated.

Another problem is when a changing current is passed through an inductor, ringing will occur. This is because the inductor does not "like" its current changed instantaneously. By measuring the voltage across the 3 Ω resistor, we found the ringing frequency to be about 20 kHz.

In order to solve the ringing problem, a snubber circuit is needed across the main coil. The snubber basically acts as a high-pass filter, so that the higher frequency components of the current will pass through it instead of the inductor. To construct the snubber, we need a capacitor and resistor, and choose them such that the corner frequency passes the ringing frequency, but doesn't pass any component of the triangle wave. Since we will be sweeping at a maximum of 3 ms (333 Hz), and assuming we need 10 harmonics to properly pass the triangle wave, we need to select the cutoff frequency somewhere above 4 kHz, but below 23 kHz. Through experimentation, we selected the values for the snubber that are shown in the Figure 4.3.

To compensate the op-amp, we can put a small resistance between the output of the second op-amp and the base of the transistor, and a capacitor between the

negative terminal and the output of the second op-amp. By performing a simulation, we can determine the optimal values.
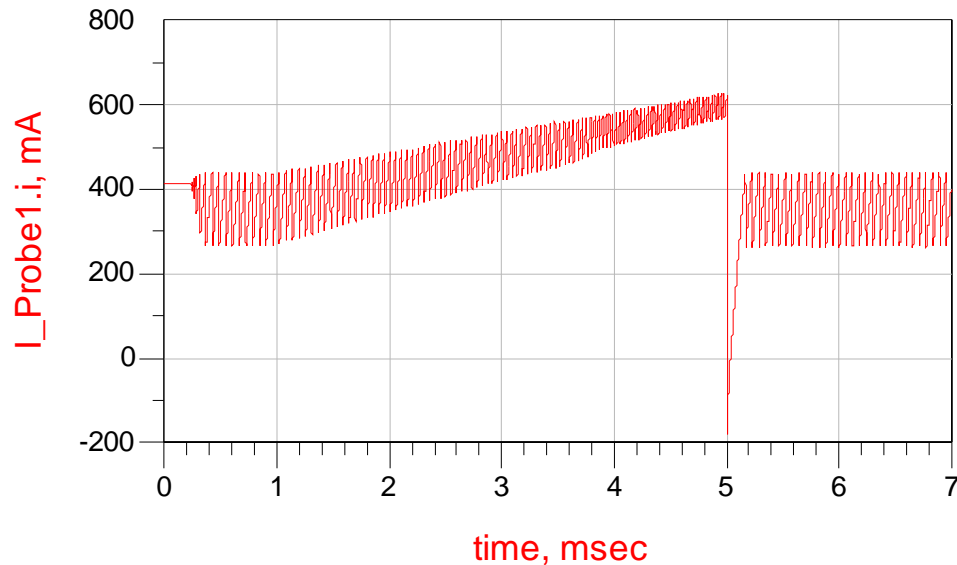
Figure 4.2: Simulation of Current through the Main Coil

Figure 4.3 shows the improved main coil driver circuit. It now includes the snubber circuit and the compensation for the op-amp. The bandwidth of the circuit is reduced to approximately 3 kHz. The free-running frequency is now set to be the midpoint between 4.5 and 6 GHz, or 5.25 GHz. Then, 1 V on the input will produce 6 GHz, while −1 V will produce 4.5 GHz.

This circuit does not show power supply filtering, which is across all power supplies and the Zener diode. In order to understand the effects of the noise, it is useful to have a complete noise analysis. Such an analysis will show what contribution the noise from the op-amps and resistors have on the voltage at V_{OUT}.
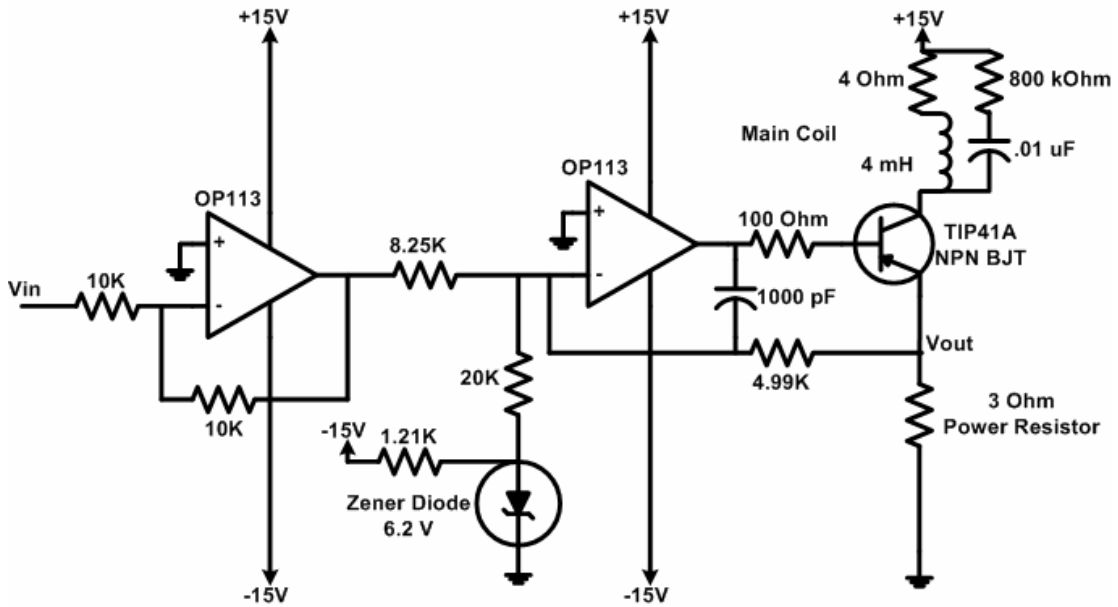
Figure 4.3: Improved Main Coil Driver with Snubber Circuit

4.1.1 Effect of Noise from Main Coil Driver

First, we can calculate the noise due to the resistances. For any resistor, we can use a noise model that is Gaussian (white), with the power spectral density given as:

$$Power\ Spectral\ Density = 4kTR \tag{4.4}$$

where $k = $ Boltzmann's constant $= 1.38 \times 10^{-23}$, T is the room temperature, assumed to be 290 K, and R is the value of the resistance. To compute the power in a particular bandwidth, we simply integrate the above expression across the bandwidth, producing:

$$Power\ in\ a\ Bandwidth = e^2 = 4kTRB \tag{4.5}$$

which is the square of the average of the mean square voltage. To perform the noise analysis, we will assume a noiseless resistor in series with a noise source as shown in Figure 4.4.
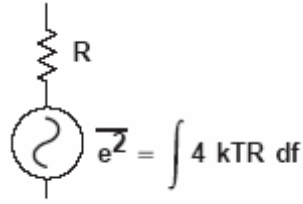
Figure 4.4: Noise Model of a Resistor [25]

We will start with the 8.25 kΩ resistor. Since the second op-amp is inverting, its gain is given by $\dfrac{-4.99}{8.25} \approx$ -.6. The mean square voltage at V_{OUT} due to this resistor is given by:

$$E_{OUT}^{2} = E_{8.25K}^{2}(.6^{2}) \tag{4.6}$$

We will assume a bandwidth of 3 kHz. Then, $E_{8.25K}^{2} = 3.96 \times 10^{-13}$, and E_{OUT}^{2} due to this resistor is 1.43×10^{-13}.

The 4.99 kΩ resistor is straightforward. E_{OUT}^{2} in this case is simply equal to $E_{4.99K}^{2}$, which is 2.4×10^{-13}. For the 20 kΩ resistor, this is the same as an inverting op-amp configuration, except R_{1} is now equal to 20 kΩ. Therefore, the gain of this inverting op-amp is $\dfrac{-4.99}{20} \approx$ -.25. Thus, the mean square voltage at the output is $E_{OUT}^{2} = E_{20K}^{2}(.25^{2})$. $E_{20K}^{2} = 3.96 \times 10^{-13}$, so $E_{OUT}^{2} = 6 \times 10^{-14}$.

To calculate the noise voltage at the output due to the 1.21 kΩ resistor, we will replace the zener diode with its equivalent circuit, which is a 10 Ω resistor in series with a voltage source which we can ground since we are doing signal analysis. We can also ground -15V source. The equivalent circuit is shown in Figure 4.5. This circuit also includes the filtering section for the zener diode. This filter consists of a series inductor and two parallel capacitors. We used a choke whose inductance is not known. Therefore, we will assume that the cutoff frequency is 3 kHz in this case as well.

The current flowing through the 4.99 kΩ resistor is $\dfrac{V_{OUT}}{4.99k}$, and the current

flowing through the 20 kΩ resistor is $\dfrac{-V_x}{20k}$. Since these two currents are equal,
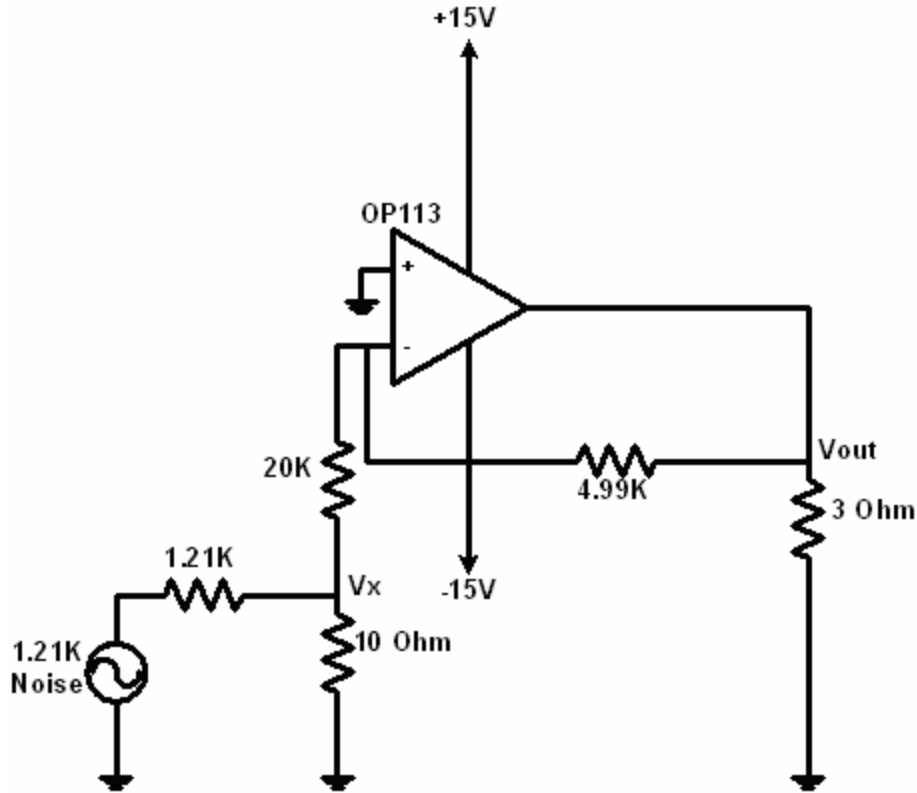
Figure 4.5 Part of Main Coil Driver Circuit

$V_x = -4V_{OUT}$. The 10 Ω and 1.21 kΩ resistor make an approximate voltage divider

for the noise source, since the impedance of the 20 kΩ resistor is much larger than the

parallel combination of the 1.21 kΩ and 10 Ω resistors. Therefore, V_x is also equal

to $\dfrac{10}{1220} \times E_{1.21k}$. So, equating the two expressions for V_x, we get that $V_{OUT} = $

$\dfrac{10}{-4 \times 1220} \times E_{1.21k}$. So $E_{OUT}{}^2 = (\dfrac{10}{4 \times 1220})^2 \times E_{1.21k}{}^2$. $E_{1.21k}{}^2 = 5.81 \times 10^{-14}$, and

therefore, $E_{OUT}{}^2 = 2.44 \times 10^{-19}$. The zener diode's noise density is approximately .08

51

$\mu V/\sqrt{Hz}$. Similar to the previous case, this time $V_X = \dfrac{1210}{1220} \times E_{ZENER}$. Equating the

two expressions for V_X, we get $E_{OUT}{}^2 = (\dfrac{1210}{4 \times 1220})^2 \times E_{ZENER}{}^2$. $E_{ZENER}{}^2 =$

1.92×10^{-11}, and $E_{OUT}{}^2 = 1.18 \times 10^{-12}$.

The two final passive components that must be taken into account are the two 10 kΩ resistors at the front end. Since the first op-amp is unity gain, both these resistors will contribute the same noise voltage to the output. The effect of one of these resistors if given by $E_{OUT}{}^2 = (\dfrac{4.99}{8.25})^2 \times E_{10K}{}^2$. $E_{10K}{}^2 = 4.8 \times 10^{-13}$, and $E_{OUT}{}^2 = 1.75 \times 10^{-13}$.

We can now analyze the effect of the op-amps. The noise model for the op-amp is shown in Figure 4.6
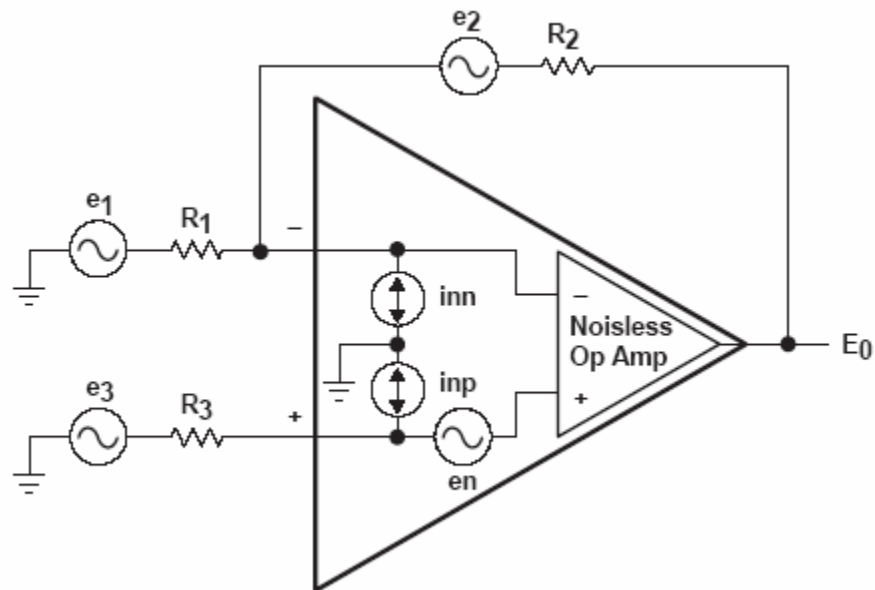

Figure 4.6: Noise Model for an Op-Amp [25]

Let us start with the second op-amp first. Looking at e_n, it will be multiplied

by $1 + \dfrac{R_2}{R_1}$. If we isolate the second op-amp from the first, then $R_2 = 4.99$ kΩ, and R_1

is equal to the parallel combination of $10\,\Omega + 20$ kΩ // 8.25 kΩ. This is approximately equal to 6 kΩ. Therefore, the mean square noise voltage at the output due to this input is:

$$E_p{}^2 = \int \left[(e_n)(\frac{R1+R2}{R1})^2 \right] df \tag{4.7}$$

Since op-amp noise is a combination of flicker, shot and thermal noise, this implies that the integral should be evaluated as a combination of $\dfrac{1}{f}$ and white noise.

It can be shown that this integral can be evaluated as:

$$e_W{}^2 A^2 (f_{enc} \ln \frac{f_H}{f_L} + ENB) \tag{4.8}$$

where $e_W{}^2$ is the white voltage noise specification, $A = \dfrac{R_1 + R_2}{R_1}$, f_{enc} is the frequency where the flicker noise density equals the white noise density, ENB is the effective bandwidth of the circuit (3 kHz) in this case), and $\dfrac{f_H}{f_L}$ is set equal to ENB.

Given this formula, we can look at the datasheet to get these parameters. Plugging them in gives us an output mean squared voltage of 2.588×10^{-13}. The noise due to i_{np} is simply 0 in our case, since R3 is 0. The noise due to i_{nn} is given by:

$$E_{nn}{}^2 = \int \left[(i_{nn})(R_2) \right]^2 df \tag{4.9}$$

Similar to the voltage above, this can be calculated using the formula below:

$$i_w{}^2 R_2{}^2 (f_{inc} \ln \frac{f_H}{f_L} + ENB)$$

(4.10)

where $i_W{}^2$ is the white current noise specification, f_{inc} is the current noise corner frequency, ENB is the effective noise bandwidth (*3kHz*), and $\dfrac{f_H}{f_L}$ is set equal to ENB.

Plugging all of this in to the equation, we get 1.224×10^{-14}.

We can now analyze the effects of the first op-amp. All of the analysis that we did for the first op-amp can be used for the second op-amp. The only difference is that the resistor values are different, and to compute the effect on the output voltage, we need to multiply the noise voltage by $\frac{4.99}{8.25}$. Using this, E_{OUT}^2 due to e_n is equal to 1.13×10^{-13}. E_{OUT}^2 due to the current noise is 1.80×10^{-14}. The following table summarizes E_{OUT}^2 due to all the noise sources in the circuit.

Assuming that all the noise sources are independent, we can combine the noise sources at the output by using the following formula:

$$E_{OUTrms} = \sqrt{E_1^2 + E_2^2 + ...} \tag{4.11}$$

This will give us the rms value of the output noise voltage. We can ignore any value that is an order of magnitude below the others. Plugging the values in Table 4.2 below into this equation gives a value of approximately 2×10^{-6}. There were some approximations made when calculating this value, as the bandwidth of the main coil driver circuit was ascertained through simulation. Ideally, in order to determine the noise bandwidth, one should construct a brick wall low-pass filter, and calculate the cutoff frequency by equating the area under the brick wall filter with the area under the actual filter response. Furthermore, in our case, the value of the cutoff frequency for the zener diode and 1.21 kΩ resistor was not known.

4.1.2 FM Coil Driver Design

The FM coil parameters are given in Table 4.3. The next phase was to design the circuitry for the FM coil driver. Since the maximum nonlinearity of the YIG main coil is .25%, this corresponds to a maximum frequency deviation of .25×6 GHz/100 = 15 MHz. Since the sensitivity of the FM coil is 310 kHz/mA, the driver should be able to source at least ±50 mA. To provide margin, we will design the driver so that it can source ±100 mA. Since ordinary op-amps can't source or sink this much

current, we need to use a special current buffer amplifier, which can source and sink high current. The OPA633 from Texas Instruments meets these specifications.

Noise Source	Value of rms noise voltage across 3 ohm resistor
8.25 kΩ resistor	3.96×10^{-13}
4.99 kΩ resistor	2.4×10^{-13}
20 kΩ resistor	6×10^{-14}
1.21 kΩ resistor	2.44×10^{-19}
Zener Diode	1.18×10^{-12}
10 kΩ resistor	1.75×10^{-13}
10 kΩ $k\Omega$ resistor	1.75×10^{-13}
Op-amp 1 Voltage noise	2.588×10^{-13}
Op-amp 1 Current noise	1.224×10^{-14}
Op-amp 2 Voltage noise	1.13×10^{-13}
Op-amp 2 Current noise	1.80×10^{-14}

Table 4.2: Noise Voltage at Output of Main Coil Driver Due to All Components

FM coil parameters	
Sensitivity, Typ.	310 kHz/mA
3 dB Bandwidth, Typ.	3 MHz
Input Impedance	.3 Ohm/1.4 uH

Table 4.3: FM Coil Parameters [18]

For the front-stage of the driver, we decided to use an instrumentation amplifier. The advantage of instrumentation amplifiers is their high common-mode rejection ratio. Since we are using an instrumentation amplifier, we must apply a differential signal at the inputs of the amplifier. One of the inputs will come from the output of the loop filter, while the other will come from the charge pump power supply. Since the voltage coming out of the loop filter cannot go below ground and cannot go above the charge pump power supply (+5 V), if we simply put the charge pump power supply into the other terminal, the difference voltage will always be positive. Since we want to be able to source and sink current, we need both positive and negative voltage at the output of the FM driver. If we divide the charge pump voltage by 2, it will be 2.5 V, and the difference between the loop filter voltage and 2.5 V will be –2.5 V to 2.5 V, which gives us the desired bipolarity.

Putting this together, we arrive at the circuit shown in Figure 4.7, which is the FM coil driver circuit. The gain of the INA111 is given by the following formula:

$$G = 1 + \frac{50k\Omega}{R_G} \qquad (4.12)$$

If R_g is removed, the gain will be 1, and this is the configuration we will use. It can be shown that the current through the FM coil is given by:

$$I_{FM} = \frac{V_+ - V_-}{25} \qquad (4.13)$$

Since, V_+ - V_- is between 2.5 to –2.5 V, the max and min current is ±100 mA, which is what we want. The purpose of the OPA602 is to get rid of an extra 1/25k term that would be in the output voltage expression if this amplifier wasn't included.

4.1.3 Loop Filter

The next critical part of the PLL design is the loop filter. The purpose of the loop filter is to filter out the spurious signals and noise from the charge pump, and present a DC voltage to the FM coil driver. The loop filter basically converts the current from the charge pump into a voltage. Because the loop filter filters out the

noise and spurious signals from the charge pump, it is desirable to keep its bandwidth as low as possible. However, an even bigger constraint is that we want to correct the nonlinearities of the main coil instantaneously. This implies that we want as wide a bandwidth as possible, wide enough so that the loop filter passes the correcting signal. The upper limit on bandwidth is given by the FM coil itself, which has a bandwidth of 3 MHz. Since we are sweeping at a maximum of 4 ms, it is reasonable to set the bandwidth so that the circuit can respond to variations on the order of 4/100 ms, or 25 kHz. Also, we definitely want to set the bandwidth of the loop filter higher than the bandwidth of the main coil driver circuit, since this is the purpose of using
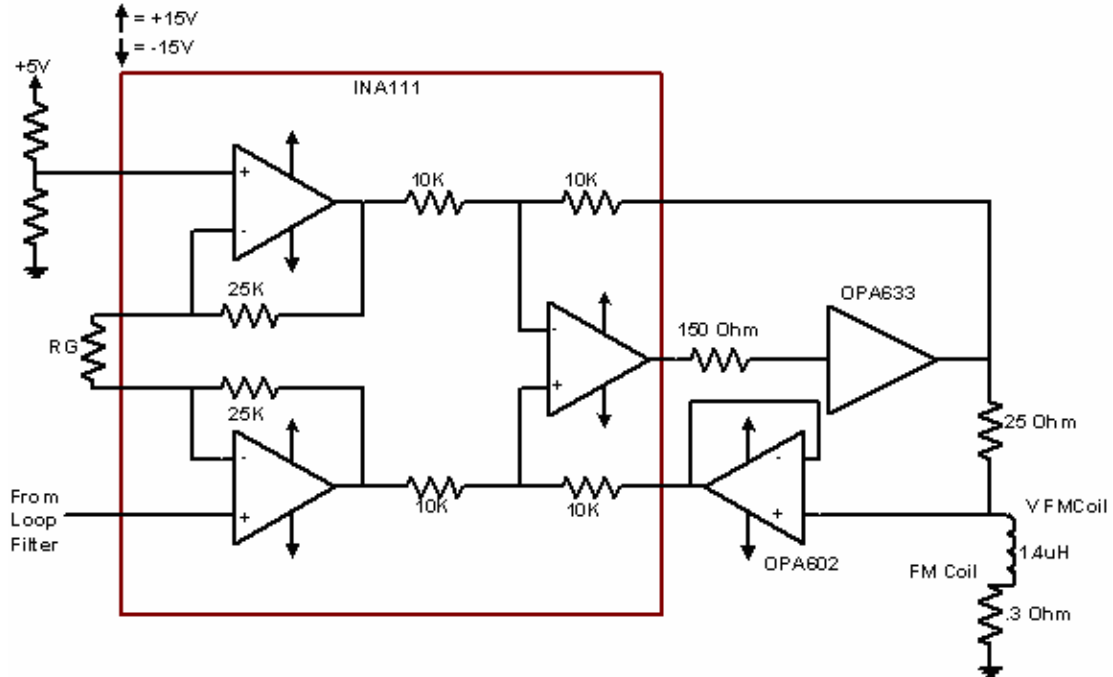

Figure 4.7: FM Coil Driver Circuit

the FM coil. The equations in [19] are used in the EasyPLL software from National. This gives the loop filter shown in Figure 4.8.

4.1.4 PLL Programming

The final major part of this system was programming the PLL chip. As mentioned before, the PLL contains three volatile memory registers, which control the comparison frequency, the R and N divide numbers, and various other functionalities. Therefore, it is useful to have a nonvolatile memory that programs the PLL whenever the power is applied. Figure 4.9 shows a block diagram of the scheme used to program the PLL.
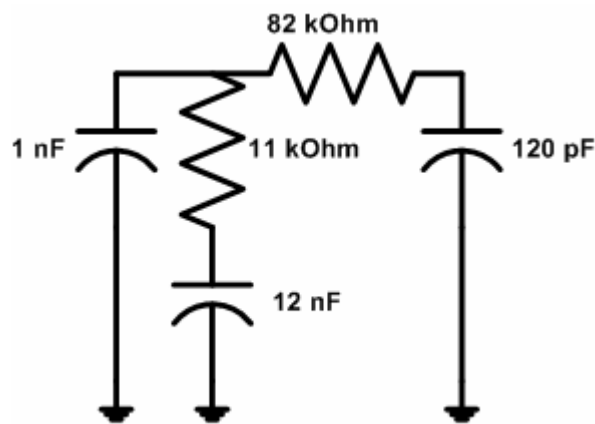

Figure 4.8: Loop Filter

When power is applied, the following sequence of steps is performed [21].

1. The two dual-voltage regulators power on the CPLD and the 10 MHz clock.

2. After some specified time, a reset pulse hits the CPLD, which initiates the programming sequence.

3. Data is serially loaded from the CPLD into the PLL at 5 MHz.

4. Once the programming is finished, the 10 MHz clock is disabled and power to it is turned off.

Each signal from the CPLD to the PLL is passed through an XOR gate for transformation of voltage levels and inversion.

58
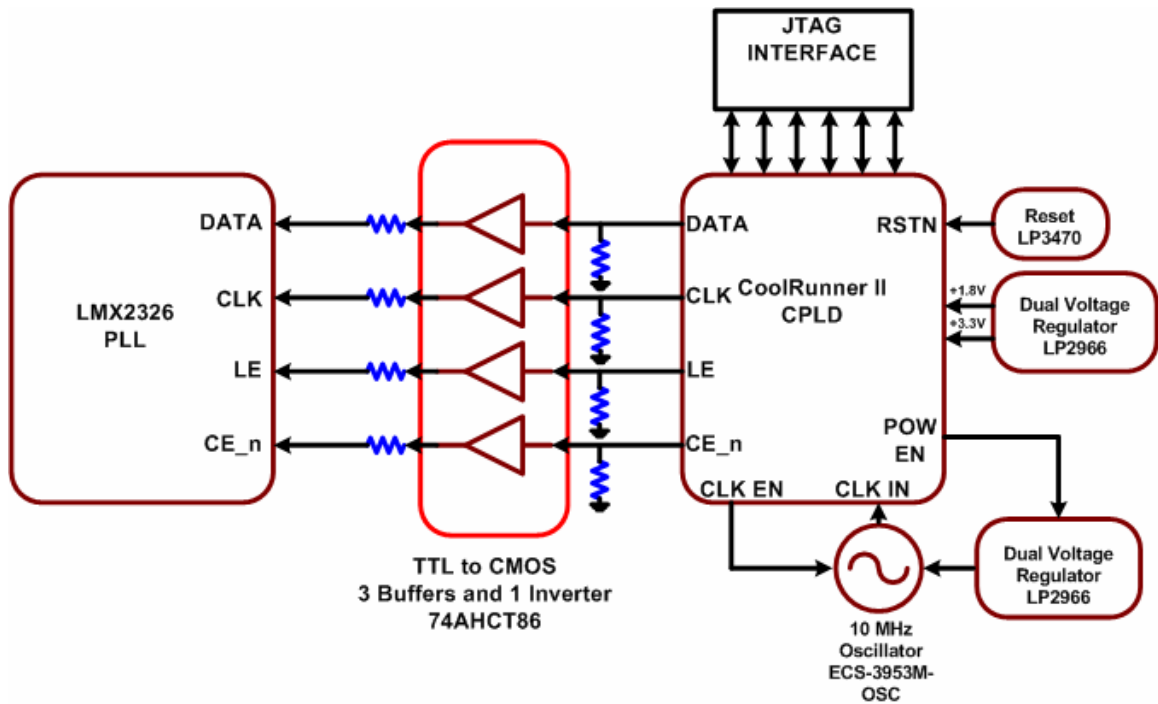
Figure 4.9: Circuit to Program the PLL

4.1.5 PLL and Oscillator Tests

Figure 4.10 shows the lock time for the PLL. The YIG output was first locked to a single frequency for 1 ms, and then, for the next 4 ms, the main coil voltage was swept while a corresponding chirp was applied as the reference.

From Figure 4.10, we see that the lock time for a single frequency is on the order of 300 μs. Right as the voltage is ramped and the chirp is applied, the loop breaks lock momentarily, only to regain lock almost immediately after. This can be seen in the figure as a jump in the voltage as the ramp begins. We tried delaying the start of the chirp with respect to the ramp, and this helped somewhat, though we

never were able to get it to lock continuously. Though this doesn't affect the performance of the PLL, it is worth exploring why the loop breaks lock.

The next evaluation was the phase noise performance of the oscillator when it is locked vs. when it is unlocked. We have already seen what effect phase noise has on the beat frequency spectrum: it causes unwanted sidelobes to appear. Figure 4.11 shows the comparison of the unlocked oscillator vs. the locked oscillator. The locked oscillator's noise characteristics are far superior to the noise characteristics of the unlocked oscillator. Also, note that the unlocked oscillator suffers from drift, which invalidates the narrowband FM approximation.
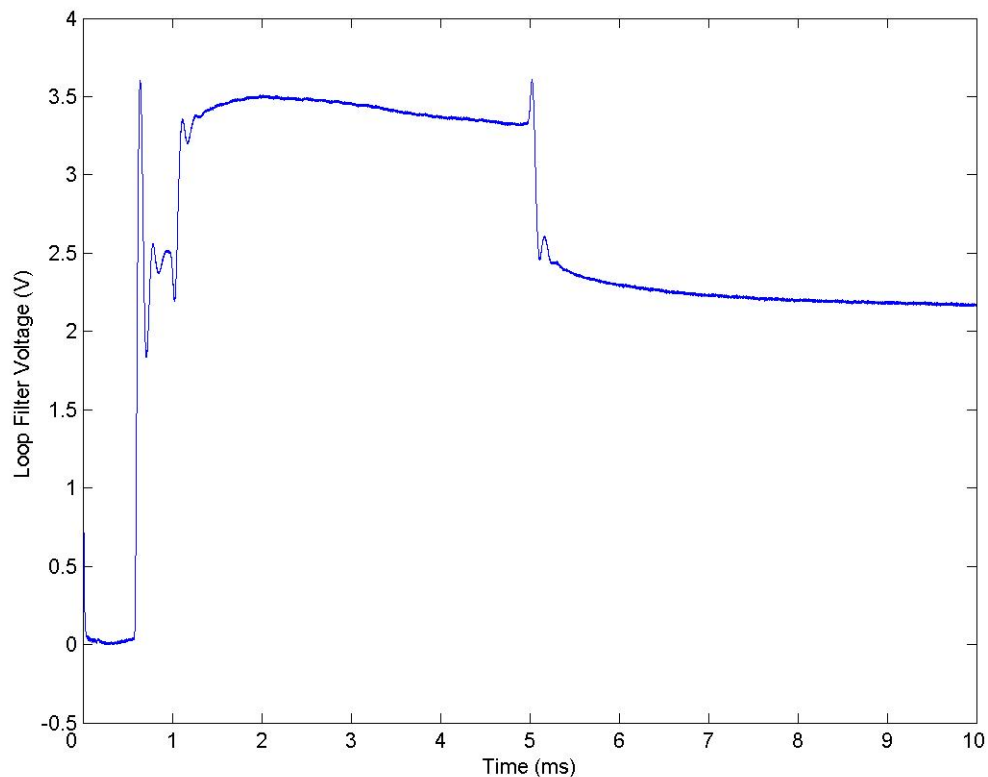

Figure 4.10: Loop Filter Voltage

We will now use the noise analysis and model for phase noise that we developed to see what affect the phase noise will have on the beat frequency spectrum. As said before, our model is valid only for frequencies outside the loop

bandwidth, which is approximately 30 kHz. Since we are locking the oscillator, the low frequency drift of the unlocked oscillator is gone, so we can now use the narrowband FM approximation developed earlier. Previously, we looked at the effect the parameter e_n has on the beat frequency spectrum. Now we want to use our calculated value of e_n and fit a curve to the locked oscillator spectrum.
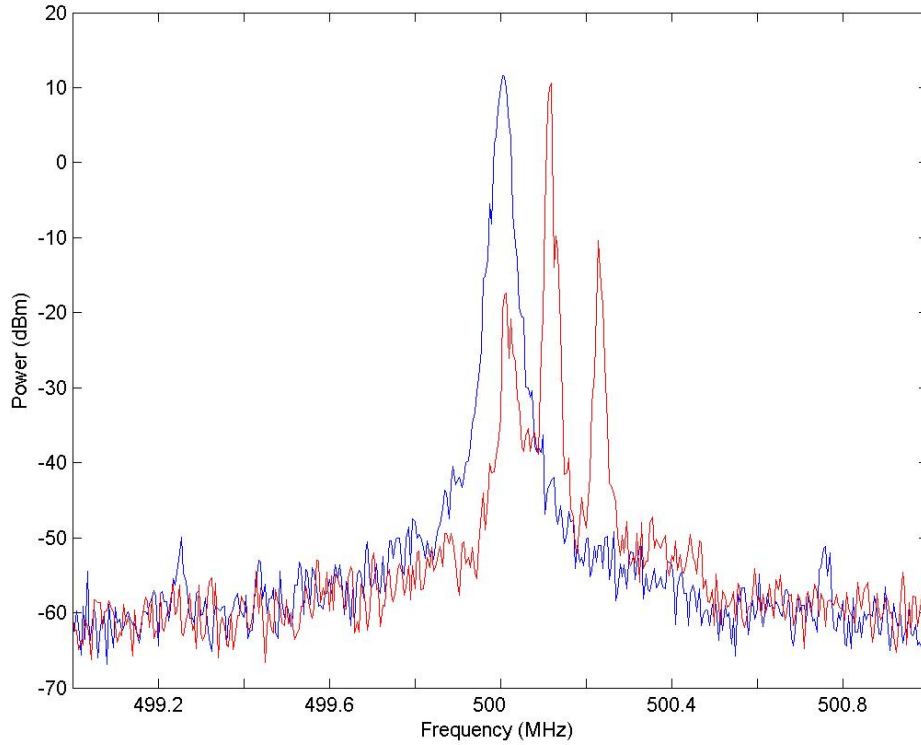
Figure 4.11: Comparison of Spectrum of Locked Oscillator (Blue) with Unlocked
Oscillator (Red)

We need to determine how far down a particular sideband is with respect to the
carrier. From equation 2.20, we saw that the phase variation could be modeled as a
sum of sinusoids spaced 1 Hz apart. This can be seen to be narrow band FM, with
$\beta = \dfrac{2\pi f_\Delta \sqrt{2} e_n}{f_m}$. The sideband amplitude is then $\dfrac{2\pi f_\Delta e_n}{\sqrt{2} f_m}$. Since we are using a YIG
oscillator, the sensitivity is given in Hz/A. Since the current used to tune the YIG
runs through a 3 Ω resistor, we can convert this to Hz/V in by dividing by 3. Thus,
the single sideband power is given by:

$$L(f_m) = \frac{K_A{}^2 e_n{}^2}{18 f_m{}^2} \tag{4.14}$$

Since all the parameters except e_n are known a priori, we can use this equation to fit a curve to the free running oscillator spectrum [26]. Figure 4.12 shows a curve fit to the locked oscillator's spectrum 300 kHz away from the carrier. The value for e_n is 7.15×10^{-8}, which is the rms voltage. This is two orders of magnitude smaller than the computed value of 2×10^{-6}. As already mentioned in the section on noise analysis, the noise bandwidth was not accurately computed, but only estimated. Also, the bandwidth limiting the zener diode and 1.21 kΩ was not properly known. There may also be some problems with the way the phase noise measurement was made. According to [22] there are some effects that must be removed when using the spectrum analyzer to measure phase noise. This was not done in this case, and thus the curve fit to the phase noise plot would be off. These considerations should be explored further.

Another interesting point about this plot is that the in-band phase noise is larger than the phase noise from the fitted curve. This is unexpected; we would expect that the loop would narrow the phase noise such that it was lower than the noise introduced by the free-running oscillator. Of course, the model we are using is simplistic, and doesn't take into account all the effects of phase noise; it only considers the effects of white, Gaussian noise. If we had a complete phase-locked loop simulation with noise models for all the components, we could find the loop gain and predict the phase noise performance of the closed loop. Such a simulation was attempted, but was not very successful. However, with proper SPICE models for all the components, such a simulation could be carried out. In any case, the effects of phase noise are minimal; from Figure 2.3, we see that using either value of e_n results in the sidebands being down by more than 30 dB, which meets our specification of 20 dB.

4.1.6 Board Level Design

A picture of the PLL board is shown below in Figures 4.13. The board was designed using Protel DXP. It is a four-layer board and is 4.2'' by 2''. It was made

using FR4 material, since there was no really high frequency trace on the board. Filtering was done when the power entered the board, at every op-amp and chip, and at the zener diode.
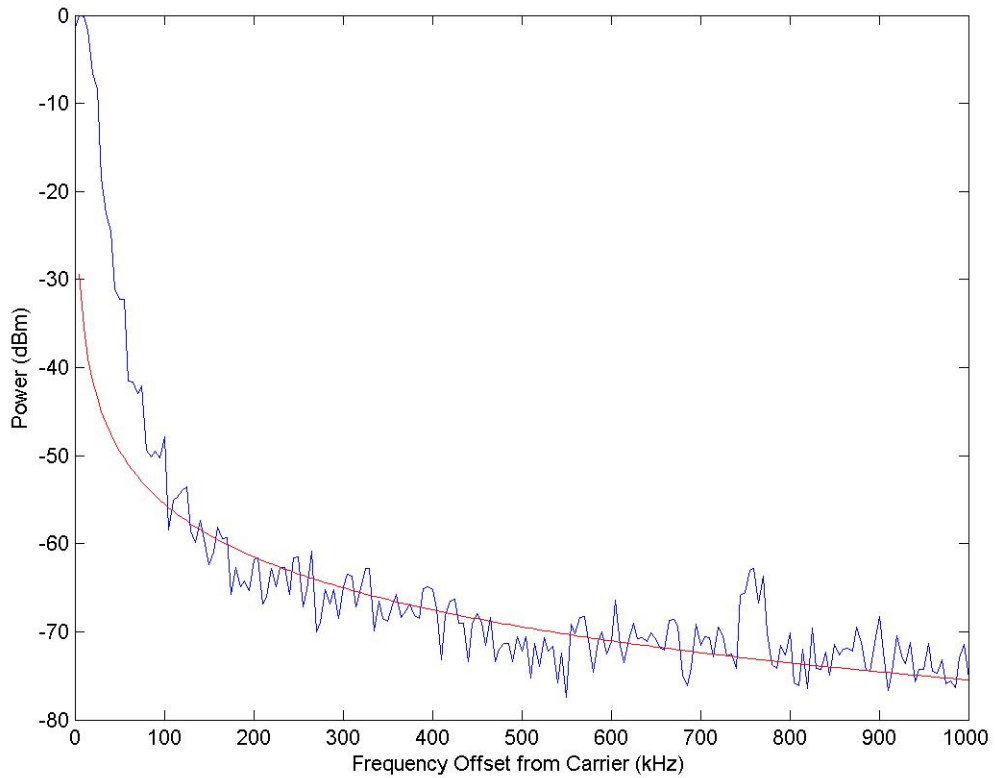

Figure 4.12: Fitting a Curve to the Phase Noise of the Locked Oscillator

4.2 AGC Design-RF component characteristics and open-loop gain variation

Figure 3.5 showed the diagram of the AGC circuit. It is shown in Figure 4.14 for convenience. The first stage of the AGC section is the down-conversion of the YIG output from 4.5-to-6 GHz down to 500-to-2000 MHz. Figure 4.14 does not include the down-conversion stage, but Figure 4.15 shows the AGC front end.
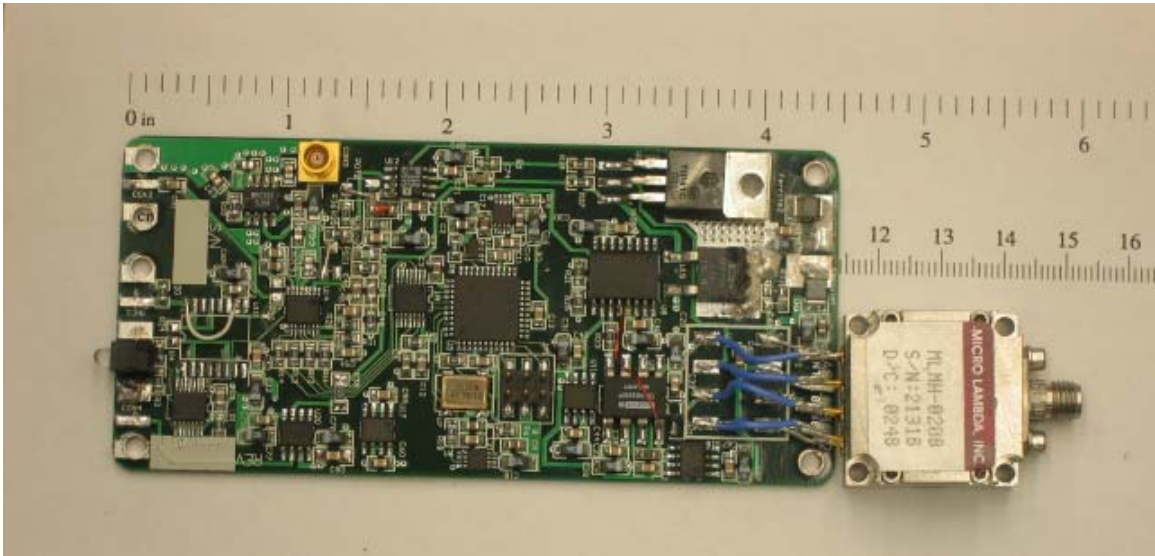
Figure 4.13: Picture of PLL board
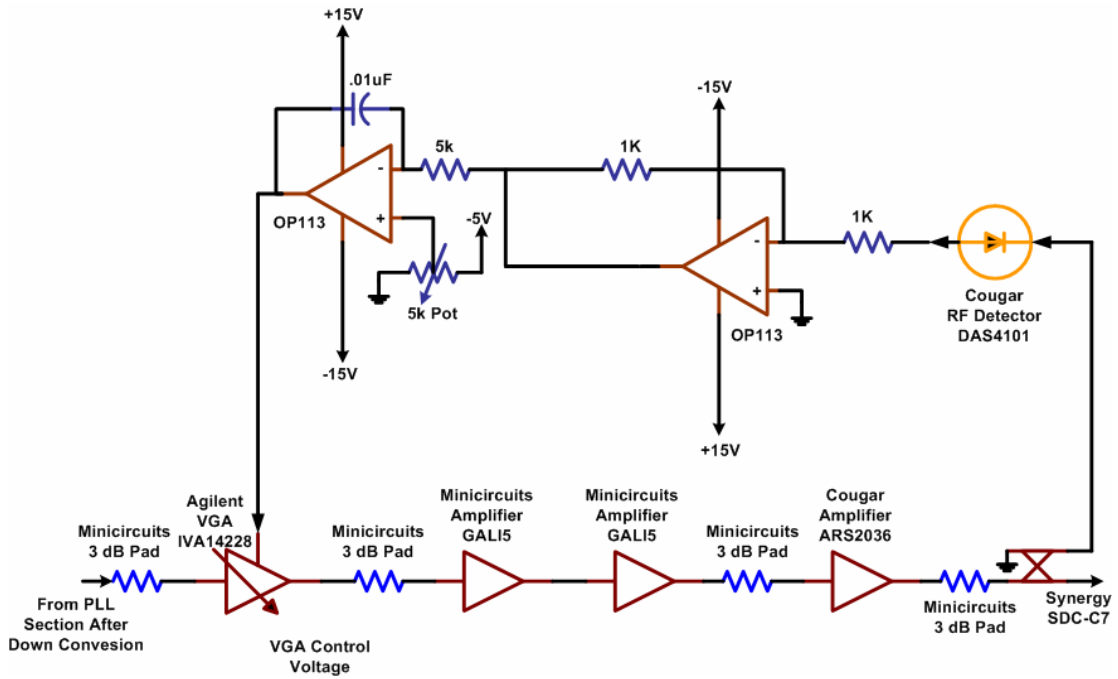

Figure 4.14: AGC Diagram
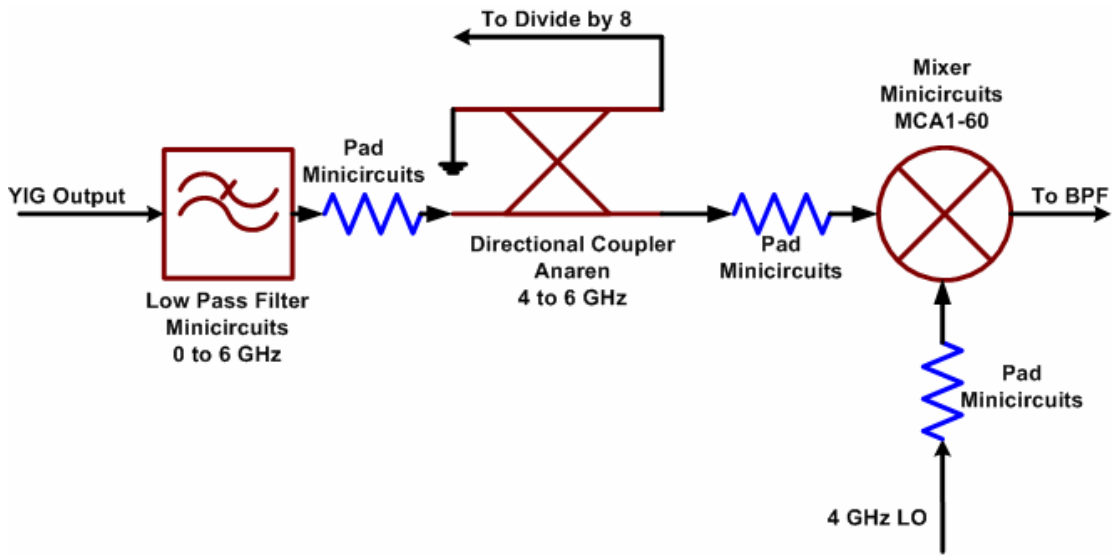
Figure 4.15: AGC Front End

This block diagram consists of a low-pass filter, to remove any harmonics from the YIG output. This is followed by a 10-dB directional coupler, to couple the signal back to the divide-by-8 component. Finally, the signal is mixed down to 500-to-2000 MHz using the 4 GHz LO. That signal is then band pass filtered. The specifications and characteristics of the Low Pass Filter are shown in Figure 4.16:

| **Minicircuits Low Pass Filter Model: LFCN-6000** PassBand (MHz): DC-6000 3 dB Frequency (MHz): 6800 Stop Band (MHz - 30 dB loss): 8500-12000 VSWR Stop Band: 20 VSWR Pass Band: 1.3 Number of Sections: 7 | |
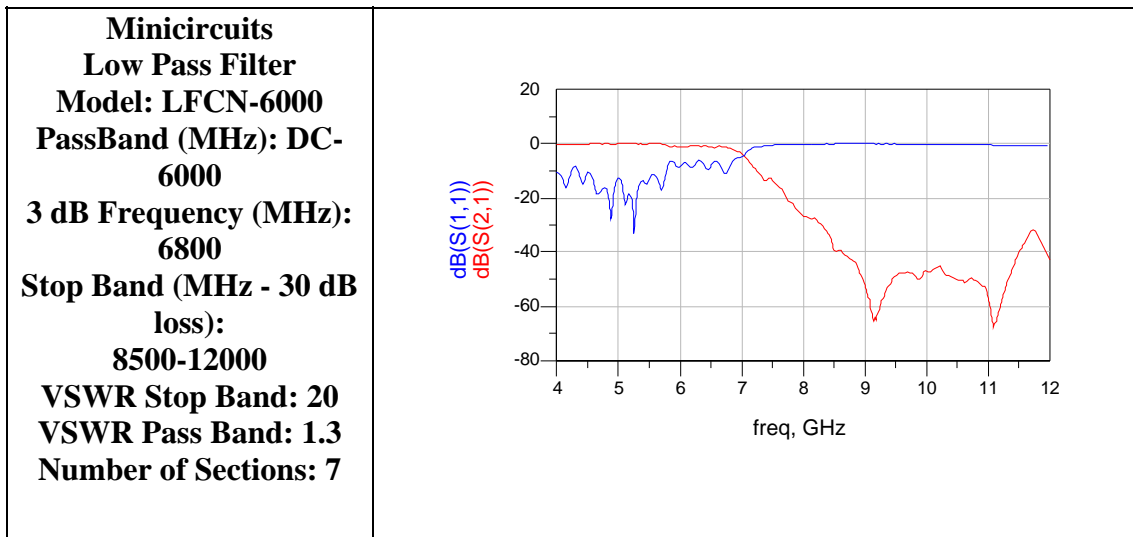
Figure 4.16: Low-Pass Filter Specifications

The next major component was the directional coupler. The specifications and characteristics are shown in Figure 4.17.

Anaren Coupler
Model: 1M80
Frequency (GHz): 4-6
Mean Coupling (dB): 10
Insertion Loss (dB): .3
Maximum VSWR: 1.33
Frequency Sensitivity (dB): .3
**Directivity (dB): 18**
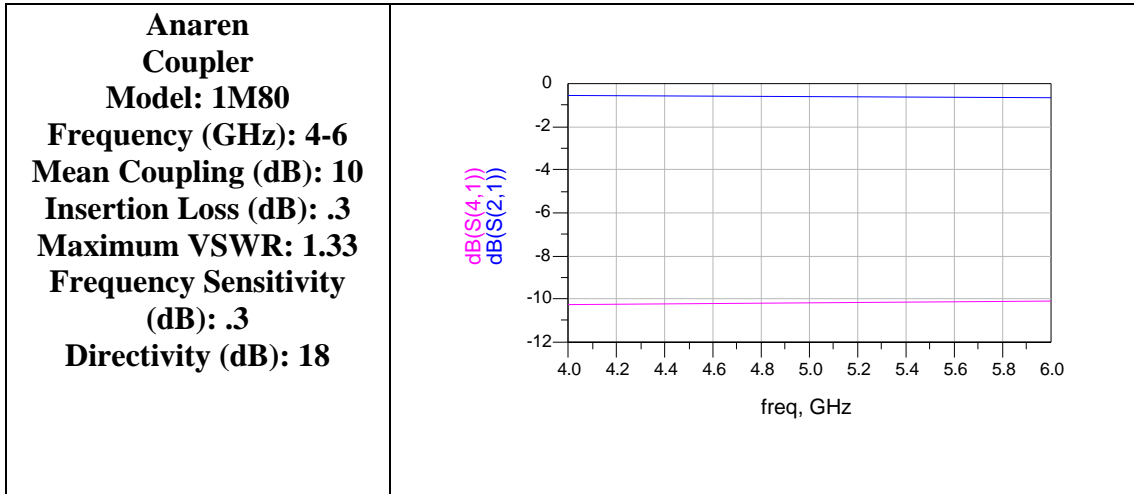
Figure 4.17: Coupler Specifications

The blue line shows the main line loss, while the purple line shows the coupling.

After getting mixed down to .5-to-2 GHz, the signal is passed through a filter. We purchased customized .5-to-2 GHz filters from Bree Engineering. The characteristics of the filter are shown in Figure 4.19.

The open loop amplifier section is shown in Figure 4.18.
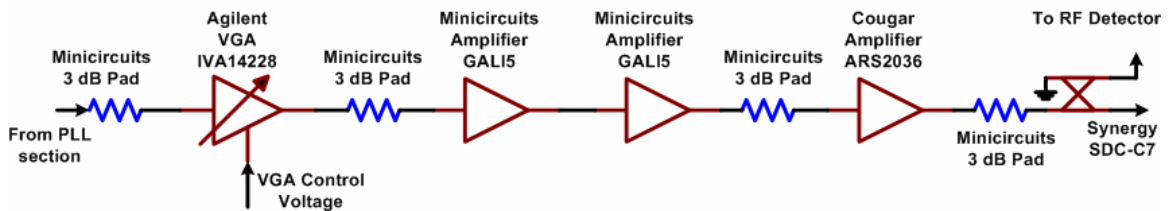
Figure 4.18: Open Loop Amplifier Section

|	
Bree Engineering Filter **Model: 800988** **Center Frequency (MHz): 1250** **Maximum insertion loss @ Fc (dB): 1.0** **Passband (MHz): 500 to 2000** **Min. Passband Return Loss (dB): 14.0** **Min. Rejection @ 350 MHz (dB): 40** **Min. Rejection @ 2500 MHz (dB): 40**	
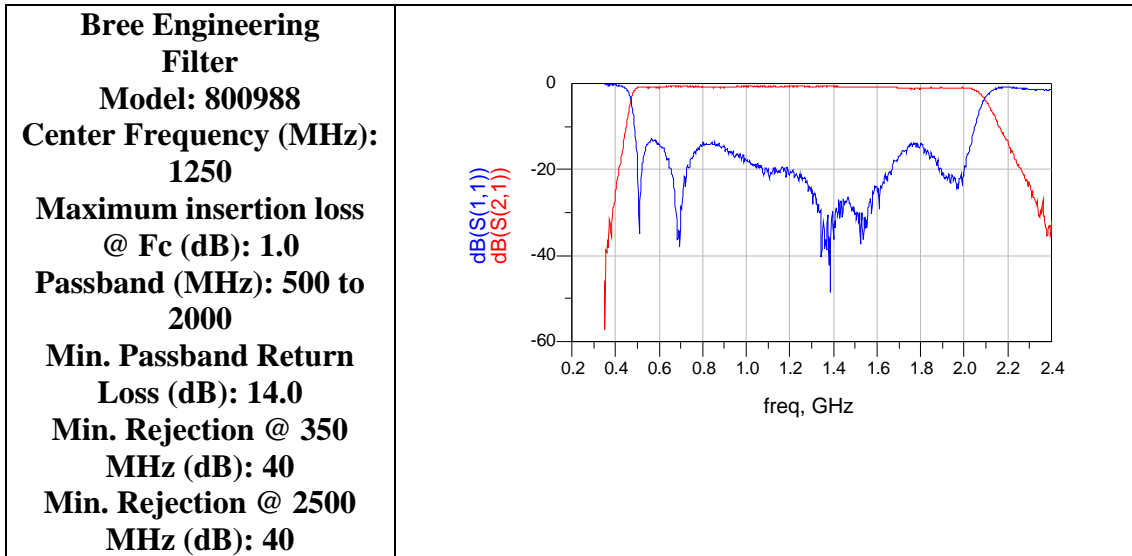
Figure 4.19: Bandpass Filter Specifications

The open loop configuration consists of a VGA followed by two GALI amplifiers, a Cougar amplifier, a coupler, and an RF detector. The first amplifier is the variable gain amplifier. The characteristics of this amplifier are shown in Figure 4.20, when the control voltage was 0 V.

The second and third amplifiers are the Gali-5 from Minicircuits. Figure 4.21 shows its specifications. From Figure 4.21, we see that the variation in gain over the bandwidth 500-to-2000 MHz, is approximately 3 dB.

The final amplifier in the chain has a high 1-dB compression point, at an input of around 20 dBm. This was necessary, since we desired to transmit 17 to 20 dBm. Its characteristics are shown in Figure 4.22.

The next two components are directional couplers from Synergy. The plots for mainline loss and coupling are shown in Figure 4.23. Figure 4.24 shows a simulation, with the appropriate pads in between, of the chain of amplifiers that shows how much variation the AGC will have to overcome. Figure 4.24 shows that the AGC has to compensate for 10 dB of open-loop variation.

Agilent Amplifier **Model: IVA14228** **Frequency (MHz): DC-2.5 GHz** **Gain(dB): 24** **Gain Control Range(dB): 34** **Compression Point (dBm): -2.0** **NF (dB): 9** **IP3 (dBm): 8** **VSWR In: 2** **VSWR Out: 2.5**	
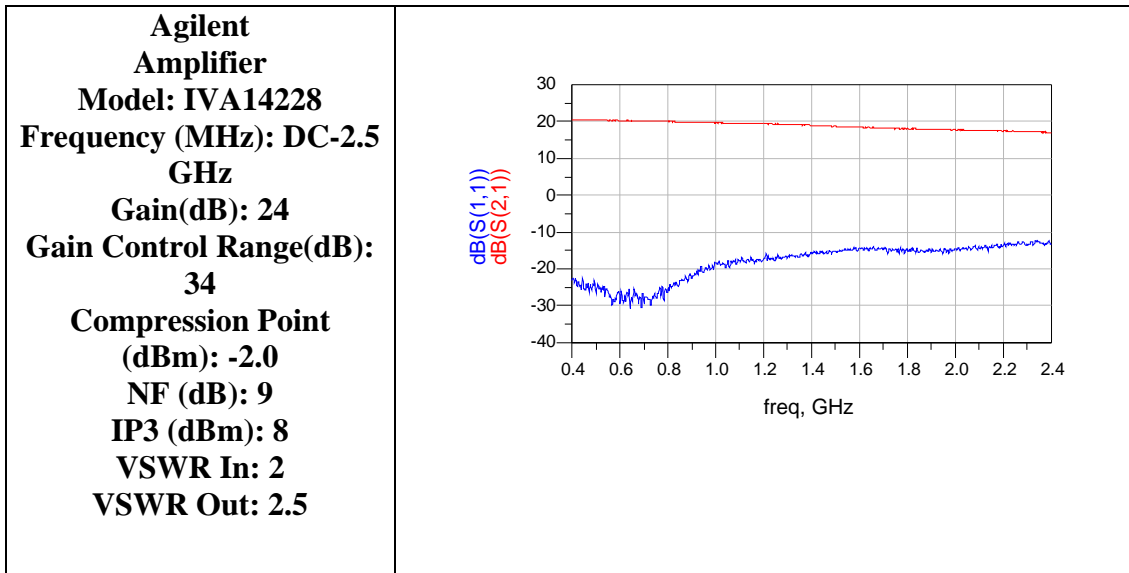
Figure 4.20: VGA Characteristics When Control Voltage is 0 V

Minicircuits Amplifier **Model: Gali-5** **Frequency (MHz): DC-4000** **Minimum Gain (dB): 16.00** **Output 1 dB Compression Point (dB): 18.00** **NF (dB): 3.50** **IP3 (dBm): 35.00** **VSWR In: 1.2** **VSWR Out: 1.4**	
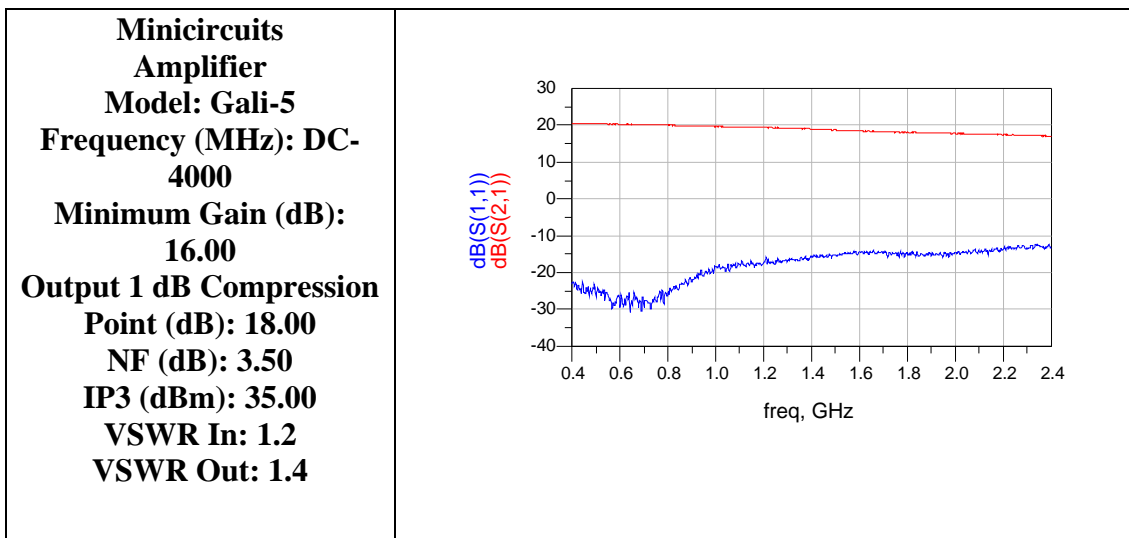
Figure 4.21: Amplifier Characteristics

|	
Cougar Amplifier **Model: ARS2098** **Minimum Gain (dB): 10.8** **Maximum Gain Flatness (dB):** $\pm.35$ **Maximum Noise Figure (dB): 5.2** **Input VSWR: 1.6** **Output VSWR: 1.6** **Power Output @ 1dB Comp. Pt. (dB): 30**	dB(S(1,1)) dB(S(2,1)) freq, GHz
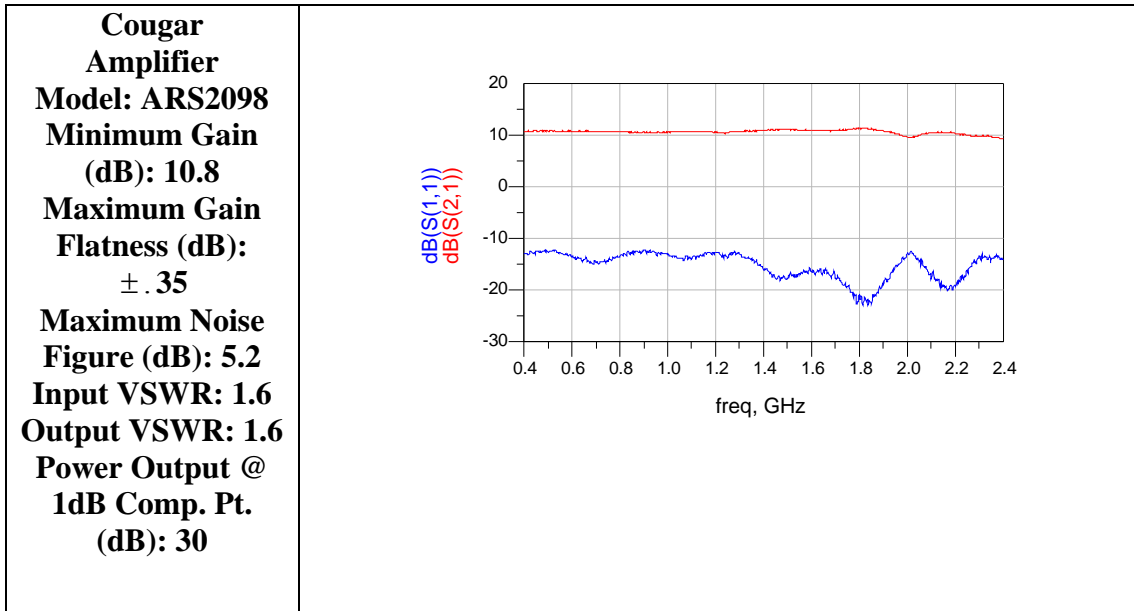
Figure 4.22: High 1 dB Compression Point Amplifier Characteristics

4.2.1 Low frequency feedback circuit

The RF detector senses power and produces a proportional voltage.

|	
Synergy Coupler **Model: SDC-C7** **Coupling (dB): 10** **Frequency (MHz): 10 to 2000** **Coupling Flatness (dB): +- 1** **Mainline Loss (LB,MB,UB) (dB):1.6,1.7,2.4** **Directivity (LB,MB,UB): 18,22,17** **VSWR: 1.3**	dB(S(3,1)) dB(S(2,1)) freq, GHz
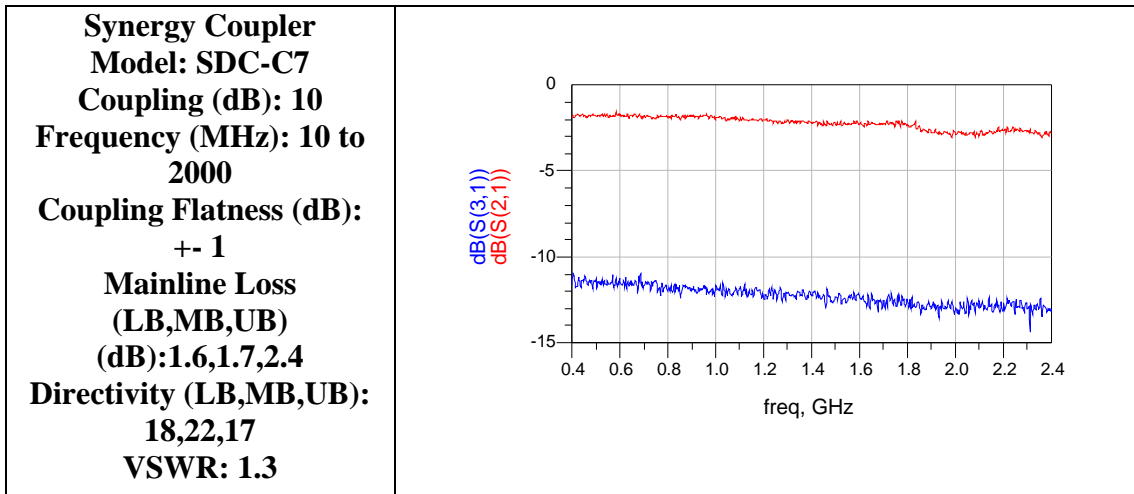
Figure 4.23: Coupler Characteristics

Therefore, if the power at the RF detector is a constant, then the power at the coupler is constant, which is the goal of the AGC. In order to achieve this, we must use an operational amplifier in the low-frequency conditioning circuit.
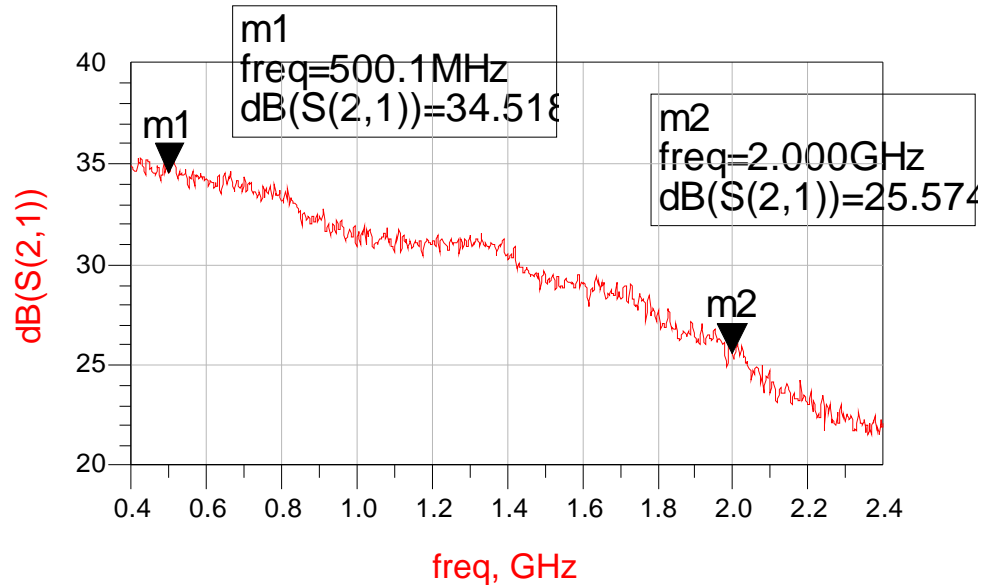

Figure 4.24: Open-Loop Gain Variation

Since feedback forces the positive and negative terminals of an op-amp to the same potential, by adjusting the voltage on one terminal of the op-amp, we can force the voltage on the other terminal to be a specific value. Figure 4.25 shows the low-frequency circuit.

Through measurement, we determined that the voltage variation coming out of the RF detector was approximately between 100 to 500 mV. Since this corresponded to the full variation of the amplifiers, we wanted the control voltage of the VGA to correct for all of this variation.
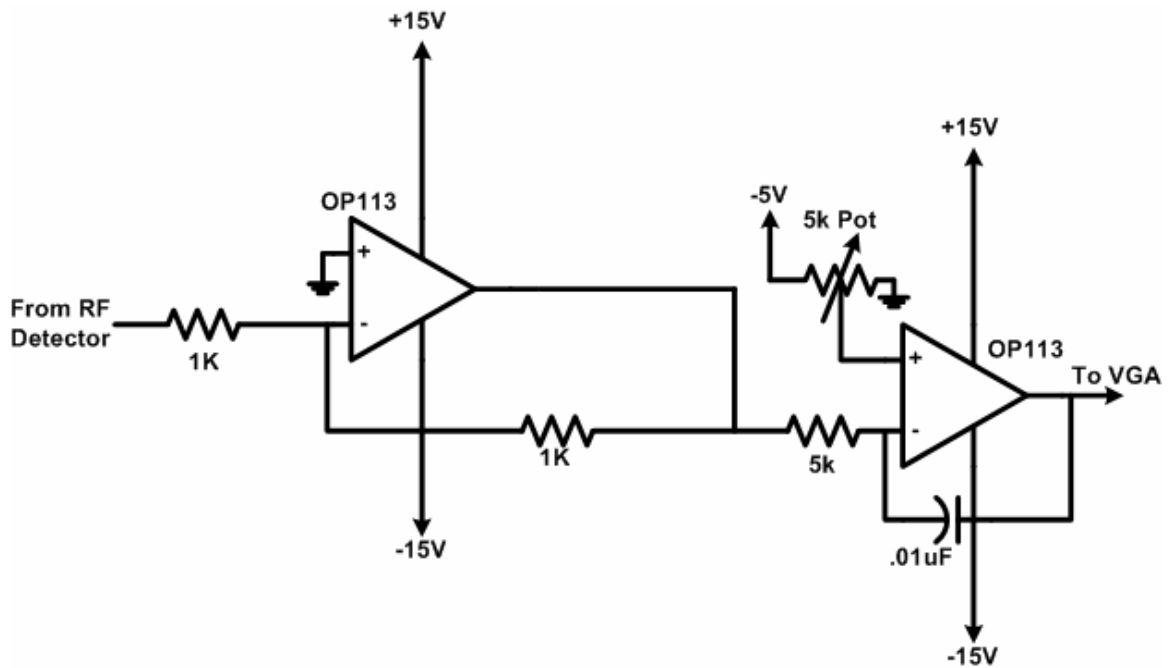
Figure 4.25: Low-Frequency Feedback Circuitry

The VGA gain decreases as the control voltage increases, and we operated the VGA at control voltages between 2.5 to 3 V. The first op-amp is simply a unity gain inverter. By adjusting the potentiometer on the second op-amp, we can get any voltage between 0 and 5 V on the positive terminal. This sets what the output voltage will be. The capacitor sets the time constant of the circuit. The output voltage will be whatever it takes to correct the variation in gain from the amplifier section.

4.2.2 AGC Results

Figure 4.26 shows the VGA voltage when the loop is correcting the amplitude variations. At the end of the curve, it can be seen that the voltage dips down. As long as the voltage does not fall all the way down, we can be sure that the loop is still correcting the amplitude variations.

The variation in output power is shown below in Figure 4.27. Thus the peak-to-peak variation in output power is approximately 1.8 dB, and the single-ended variation is .9 dB. Ideally, we should Fourier expand this signal to see the peak-to-

peak variation in the sinusoidal components which make it up. For simplicity, we will assume our previous analysis is valid for this signal as well.
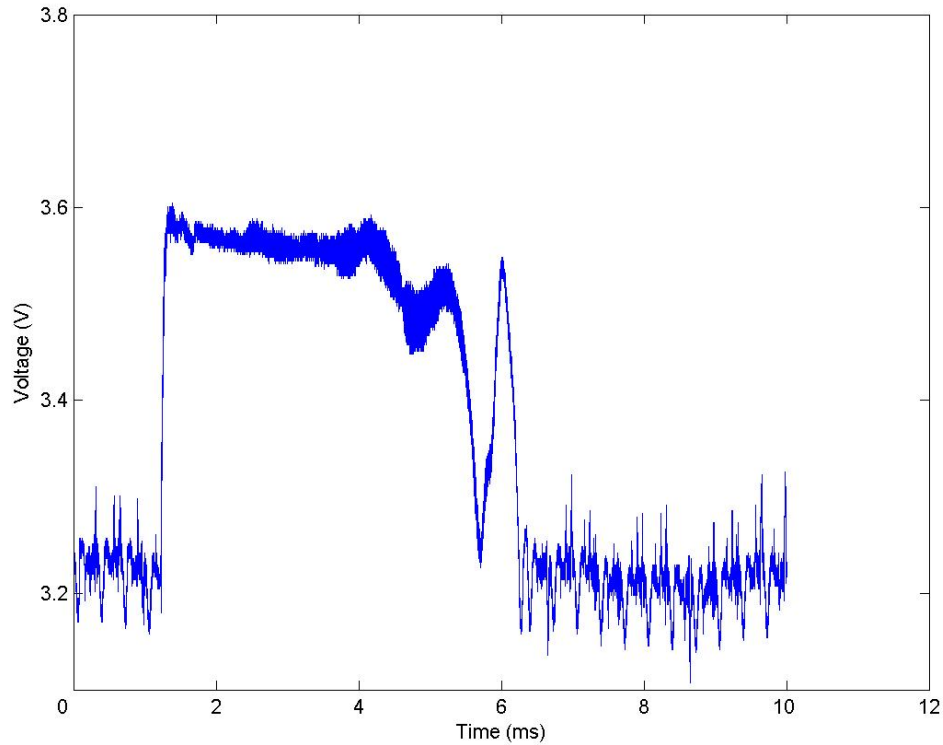

Figure 4.26: VGA Control Voltage as a Function of Time

This means that the sidebands due to amplitude modulation alone will be down by about 25 dB, which meets our specification of 20 dB.

4.2.3 Schematic and Board Layout

Since the board had to support frequencies from 500 MHz to 6 GHz, we used Rogers4350 material to lay out the board. The low-frequency feedback section was done on FR-4 material to reduce the cost by avoiding a four-layer board. The low-frequency board plugs-on to the high frequency board. Figures 4.28 and 4.29 show pictures of the high and low frequency boards.
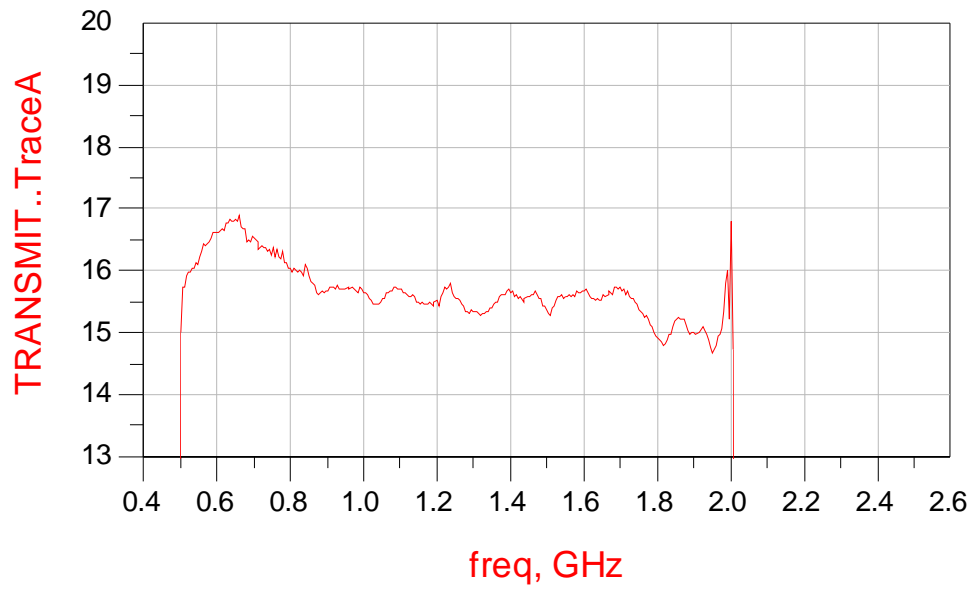
4.27: Variation in Output Power after Correction
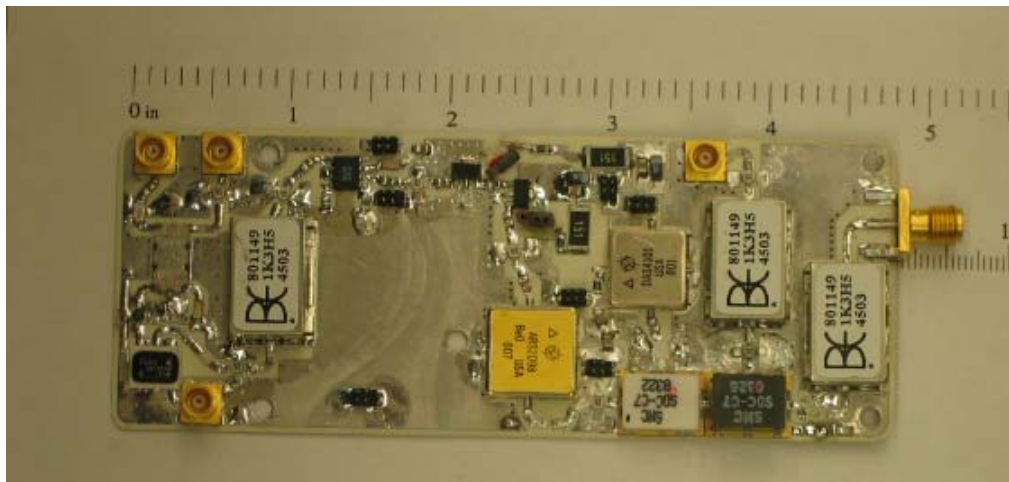
Figure 4.28: Picture of High-Frequency AGC Board
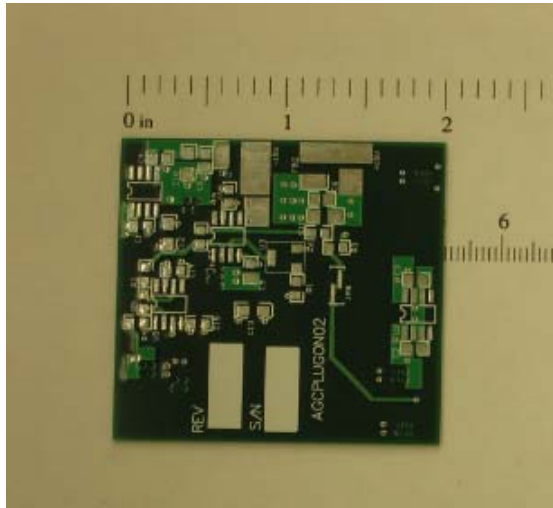
Figure 4.29: Picture of Low-Frequency AGC Board

4.3 PLO Design-Schematic and Board Layout

Figure 4.30 shows a picture of the PLO board. We laid out the board on Rogers4350 material since we have a 4-GHz signal running through the board. Careful attention was paid in making sure that all unused portions of the board were grounded with a sufficient number of vias.
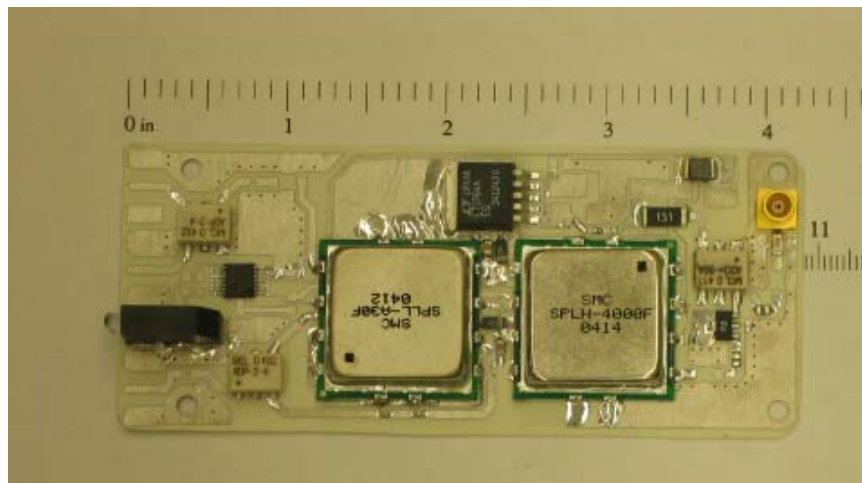

Figure 4.30: Picture of PLO Board

4.4 RF Section Design

The diagram of the RF circuit is shown in Figure 3.7. The main consideration in designing the RF section was ensuring that the RF power at the mixer is at least 15 dB below the LO power. Since the LO power was around 4 dBm, the RF power should be below −11 dBm. We designed this system assuming that the transmit and receive antennas would be mounted on opposite sides of the tracked vehicle. In this case, we expected the returns from the top layers to be around −30 dBm, due to the attenuation caused by the vehicle [19]. The overall gain of the front end before the mixer is 20 dB, which puts the RF power at a maximum of −10 dBm.

The characteristics of the High-Reverse Isolation Amplifier are shown below in Figure 4.31.

| **Cougar Amplifier** **Model: ARS2036** **Minimum Gain (dB): 26.5** **Maximum Gain Flatness (dB):** $\pm .35$ **Maximum Noise Figure (dB): 5.5** **Input VSWR: 1.7** **Output VSWR: 1.7** **Power Output @ 1 dB Comp. Pt. (dBm): 14.5** **Reverse Isolation (dB): 45** | |
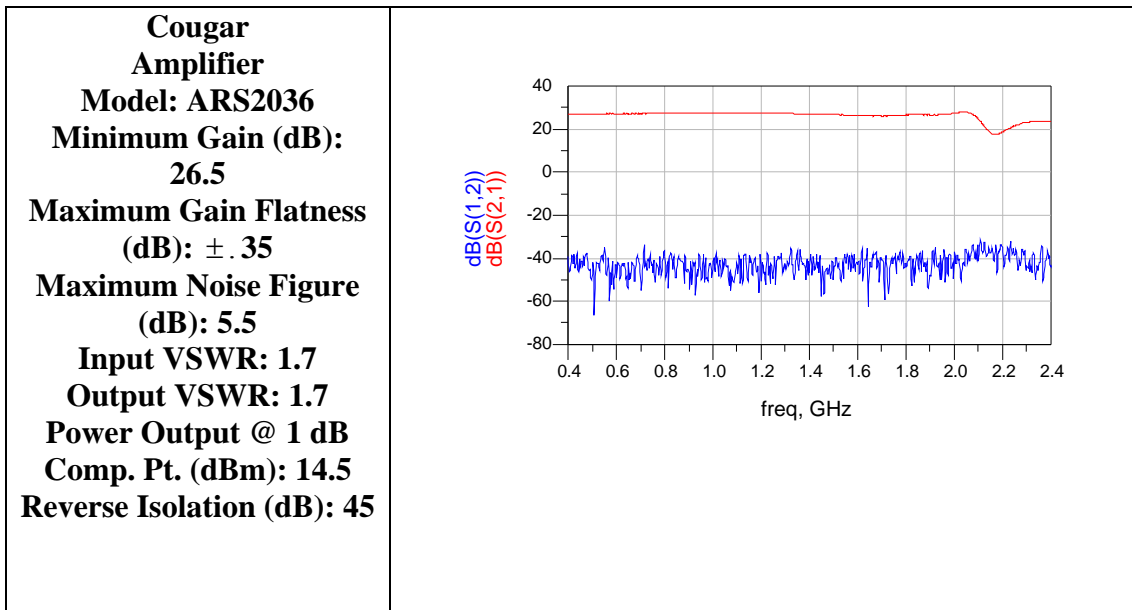
Figure 4.31: Characteristics of High-Reverse Isolation Amplifier

The red trace shows the amplifier's gain, while the blue trace shows the reverse isolation.

4.4.1 RF Section Schematic and Board Layout

This board was laid out on Rogers4350 material because the maximum signal frequency through it was 2 GHz. The board is a two-layer board with one +15 V power supply. Figures 4.32 shows a picture of the board.
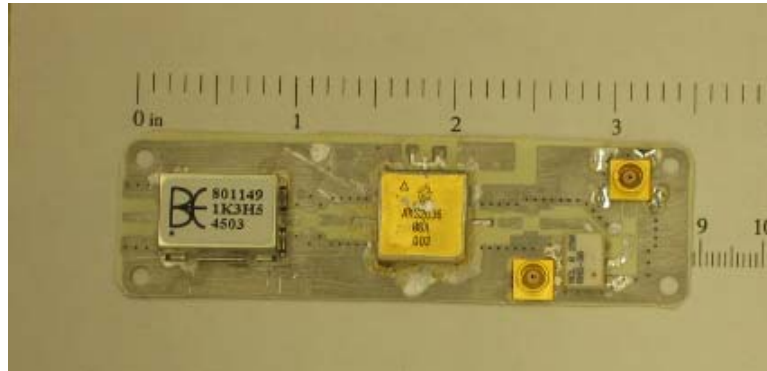

Figure 4.32: Picture of RF Section of the Receiver

4.5 IF Section Design

The IF section circuit is shown in Figure 3.8. As stated in section 3.2.5, the main consideration is ensuring that the antenna feed-through signal and signals from the top layers do not saturate the A/D converter. Any saturation is undesirable because harmonics are produced. To calculate the beat-frequency due to the antenna feed-through, we assume that the transmit and receive cables are both 3 m, and the antennas are placed 1 m away from each other, the total length is about 7 m. Using equation 2.3, the beat frequency of the antenna feed-through signal is at 9 kHz. We also need an estimate of the power from this feed-through signal. When we made this estimation, we assumed that the transmit and receive antenna would be mounted on either side of a tracked vehicle. From [19], it was assumed that the tracked vehicle would cause the feed-through signal to be approximately –30 dBm. Using this estimate, we designed the Gaussian high-pass filter to have 75 dB of attenuation at 9 kHz. The power of the feed-through signal going into the A/D converter would be

around –40 dBm, which won't saturate the A/D converter. Figure 4.33 shows the frequency response of the filter

In order to decide what kind of op-amp we should use, we need to know the beat frequency of the furthest return. If that distance is 200 m, the beat frequency will be around .7 MHz. Therefore, we used a high gain-bandwidth product op-amp, the OPA687 from Texas Instruments. In section 3.2.1, we calculated that the total gain of the receiver to be around 58 dB. The op-amp is operated as a non-inverting amplifier. Its gain is 55 dB. Finally, the low-pass filter has a cutoff frequency of 5 MHz.
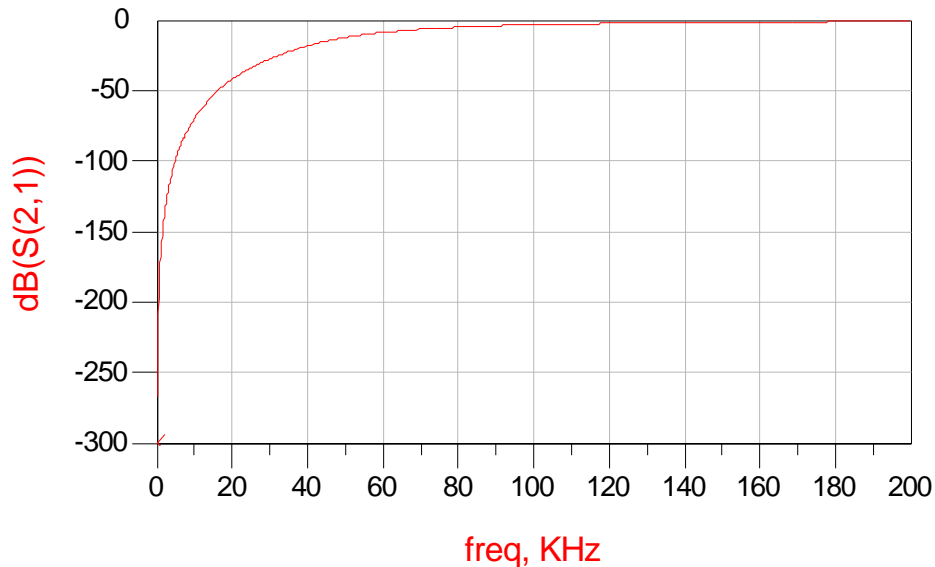
Figure 4.33: Gaussian Filter Frequency Response

4.5.1 IF Section Schematic and Board Layout

Particular attention had to be paid when laying out the board because of the high speed op-amp. Such op-amps tend to oscillate when small capacitive loads are present. Therefore, the ground plane around the chip's pins was removed, to get rid of any stray capacitance. Figures 4.34 shows a picture of the IF section.
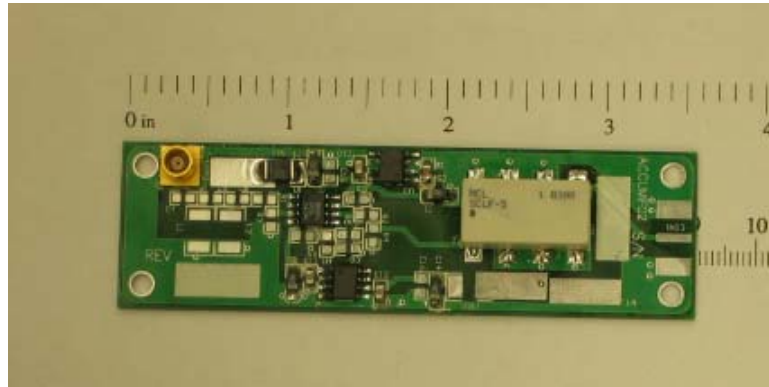
Figure 4.34: Picture of IF Section of the Receiver

CHAPTER 5

EXPERIMENTS AND RESULTS

5.1 Introduction

This chapter provides a summary of results obtained with the prototype system. The data was collected at NGRIP during the 2003 field season. This chapter also presents sample results of data collected with the operational system at Summit camp in Greenland during the 2004 field season. The results show that we can map layers to a depth of about 200 m with fine range resolution.

5.2 First Generation Radar Tests and Results

We developed a prototype system for optimizing system performance. It was housed in a large 18'' by 24''by 7'' rack-mounted chassis. We used a dual output (+15V and −15V) linear power supply. We developed radar subsystems using surface mount components on a single FR-4 board and housed in an RF tight enclosure. We connected subsystems with mini-bend SMA cables. We used SMA connectors and cables to connect the RF subsystem to the antenna, and the IF subsystem to the digital subsystem.

The radar was tested during the 2003 field experiment at NGRIP. The signal processing involved applying a Hanning window to the data to reduce the range sidelobes and taking a Fourier Transform of the windowed data to obtain a spectral plot. Since there is a $1/r^2$ roll-off in power with range, we low-pass filtered the spectral data using a filter with a very low cut-off frequency [19]. The original spectra was then multiplied by the inverse of the low-pass filter response, to correct for the gain. We applied a median filter along the layers to obtain a smoother image. Figure 5.1 and 5.2 shows some of the results obtained.
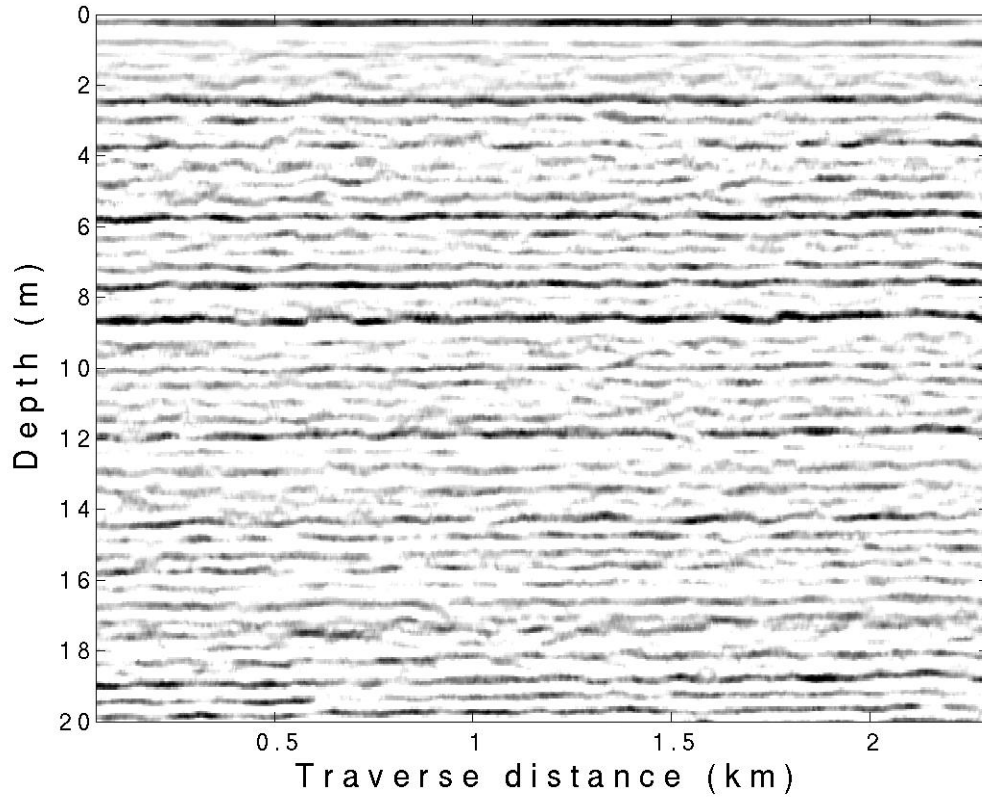
Figure 5.1: The First 20 m of Internal Layers at NGRIP

These two pictures show data taken at NGRIP. The top picture shows the top 20 m of layers, while the bottom shows layers from 138 to 160 m. From the figures we can see layers up to 160 m along this traverse. The prototype system was not optimized to generate fast sweep. It was operated with a 4 ms sweep rate and 100 coherent integrations were performed to reduce the data volume. The antennas were mounted on top of a tracked vehicle, which was driven at speed of 10 km/hr. The fading is the result of random phase variations over the integration period caused by the vibration of antennas and surface undulations.

We can estimate the water equivalent accumulation rate by using formula 5.1.

$$A = \frac{dR}{dT} \frac{\rho_{layer}}{\rho_{water}} \tag{5.1}$$

where A is the accumulation rate, dR/dT is the increase in ice thickness per year, ρ_{layer} is the average density between two layers, and ρ_{water} is the density of water [8].
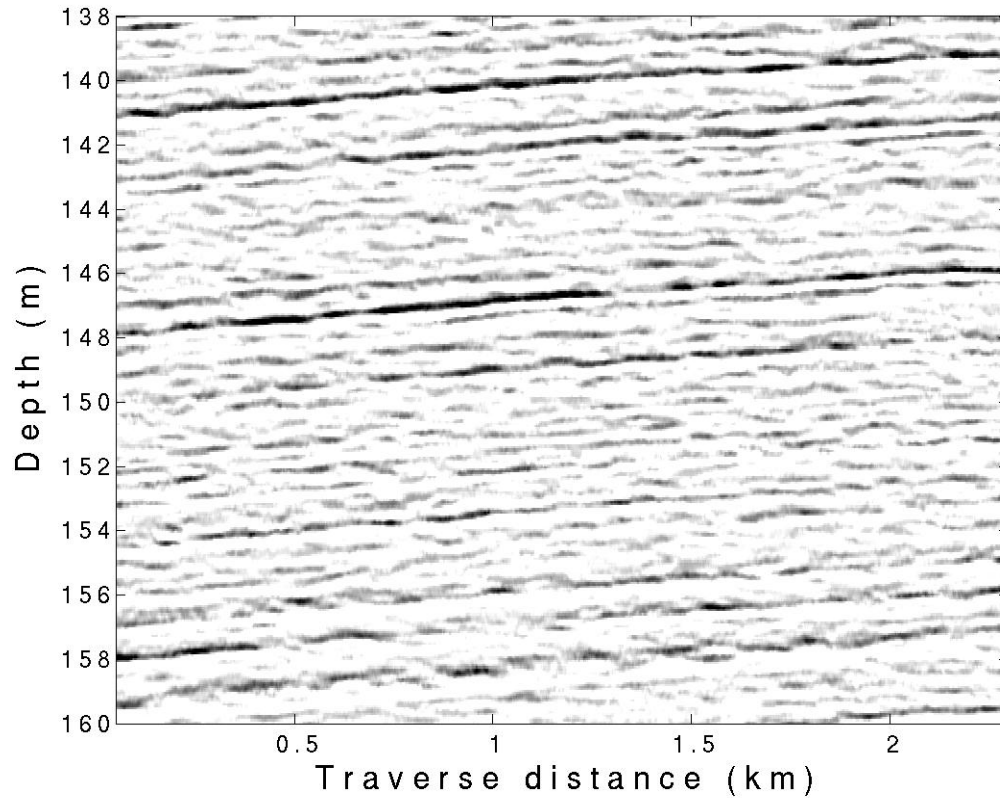

Figure 5.2: Deep Internal Layers from NGRIP

We will estimate ρ_{layer} from ice core data. Taking an average of a few layers, we find ρ_{layer} to be .455 g/cm^3, and ρ_{water} is 1 g/ cm^3. Looking at Figure 5.1, we estimate that there are approximately 5 layers every 2 m. Since each layer corresponds to one year, this is an average of .4 m/year of accumulation. Multiplying this by the density ratio, we get a water equivalent accumulation rate of 18.2 cm/year, which compares favorably with previous estimates of 17 cm/year [8].

5.3 System Improvements

After the first field season, we noticed several areas that could be improved. Specifically, we wanted to build a lower-noise driver circuit, since we the YIG is very sensitive to noise. We also wanted to improve the performance of the AGC, in order to reduce amplitude fluctuations over the entire bandwidth. Finally, we wanted to fit the entire radar into one CompactPCI chassis.

The size of the radar was significantly reduced. We ended up needing just one CompactPCI card made of aluminum. The size of the CompactPCI card placed severe restrictions on the length and width of the board, since the entire CompactPCI card is just (give length, width), and we had five modules to fit in. Additionally, since the height of the card is .5 to .6 inches, we needed to find components whose height was no more than .4 to .45 inches. Some of the layout considerations are presented below:

- Since all input and output signals had to come from the front panel, we designed the boards to utilize the length of the card, and shortened the width. In other words, we tried to make the boards as long and narrow as possible.

- Since the power connections come from the back, we designed the boards so that the power entry point is close to the power connection.

- To interconnect the boards, we used MCX connectors, which work up to 6 GHz. These connectors face up, allowing them to be placed anywhere on the board. We had to carefully place them to make it easy to connect cables from one module to another.

- Since the card is made of aluminum, it serves as an ideal heat sink. To utilize this, we placed many vias underneath devices for heat sinking.

- We provided extra filtering to ensure that switching noise didn't corrupt sensitive analog and digital circuitry. Power supply filtering was done in three places: a power filtering board was placed between the power supply and module; power supply filtering was done when the power came into each board, and

power supply filtering was done at each component.   The picture below shows the operational radar system.
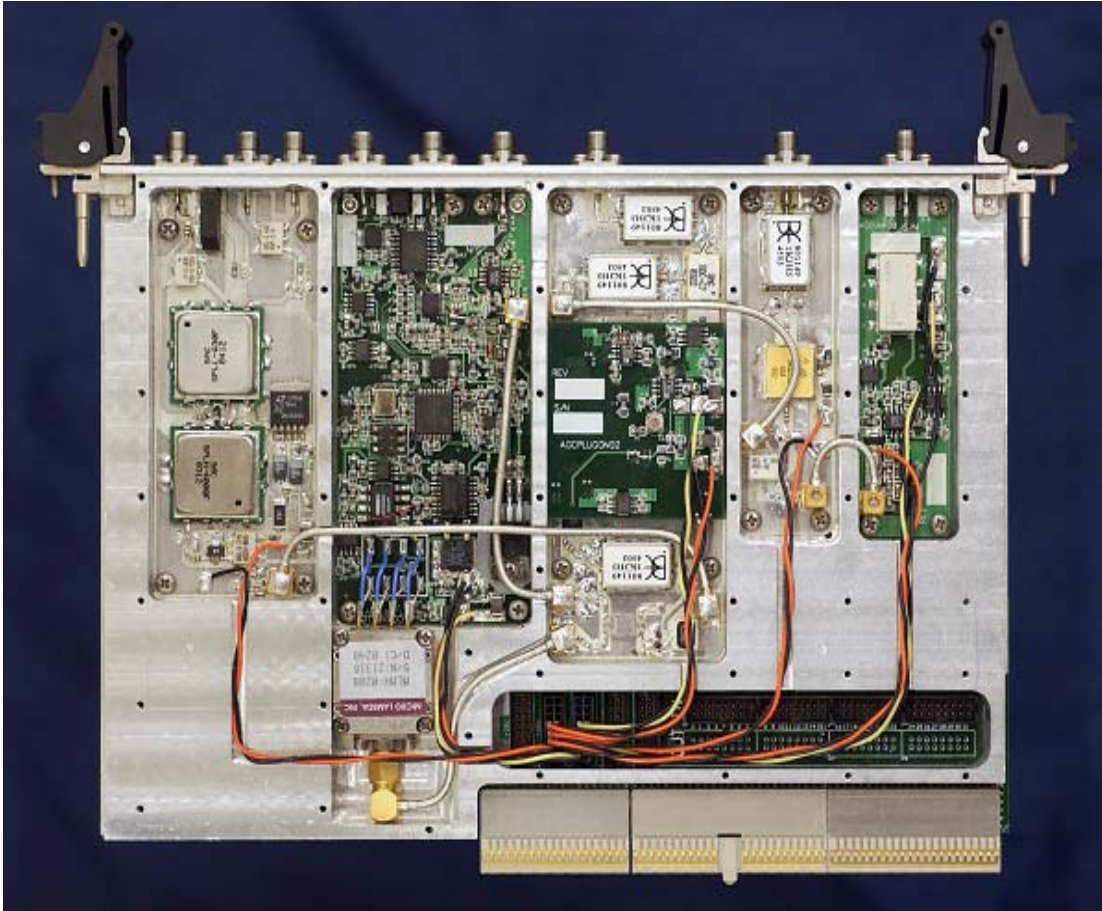
Figure 5.3: Improved Radar

5.4 Second Generation Radar tests and Results

We took two delay line measurements and deconvolved the delay line and system response. Figure 5.4 shows the system response plot against the uncorrected spectrum.   Both spectrums are taken with a Hanning window.   The uncorrected response has sidelobes that vary between –28 and –35 dB below the main lobe.   There is also a bump that is –17 dB below the main lobe.   The blue curve shows the spectrum when the effects of the delay line are removed. The sidelobes are –35 dB

down, which is good, however, there is still some artifact of the system which causes a bump –20 dB below the main lobe. There are some other small peaks in both spectrums which are likely cause by intermodulation products. Figure 5.5 shows the block diagram of the test setup. There will be some power reflected at the boundary of the transmitter block and the delay line. The peak at 39.1 kHz could be caused by the reflection from the delay line or from some internal reflection in the transmitter block. The peak at approximately 45 kHz would then be a third order product, since the main peak is at approximately 42 kHz, and $2 \cdot 42 - 39 = 45$ kHz.
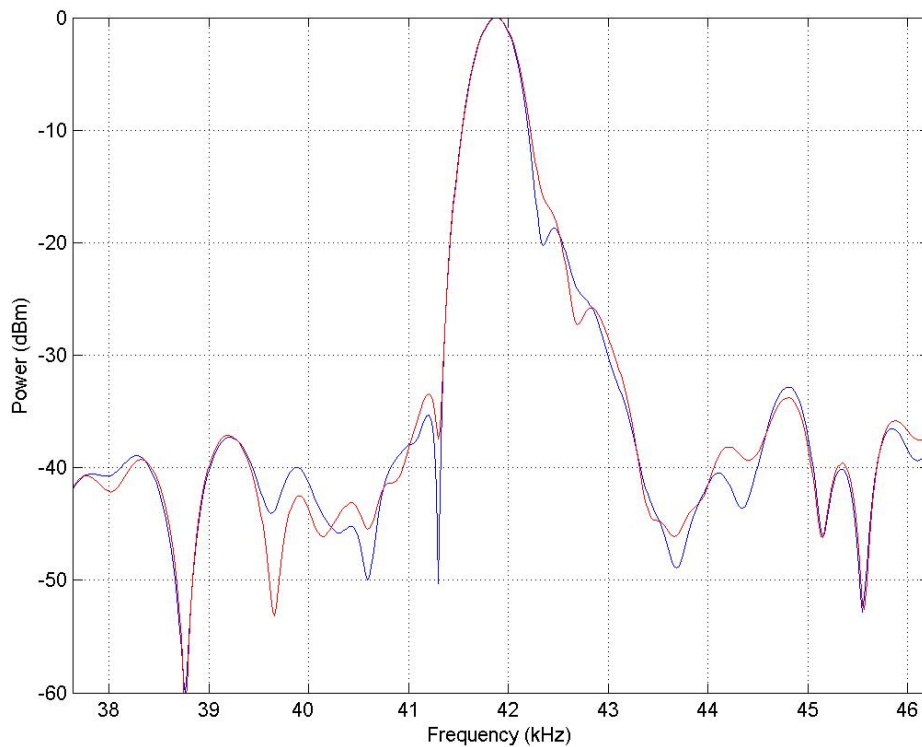

Figure 5.4 : System Response (Blue) vs. Uncorrected Response (Red)

The peak at 42.5 kHz which is 20 dB below the main peak could be caused by phase errors in the system. It could also be a multiple reflection. Since we are using

a phase-locked loop configuration, we wanted to make sure that this effect was not coming from the oscillator, since its phase should be close to ideal. We saw that the effects of phase noise would be negligible, so this can't be the source of the problem. Also, the effects of amplitude modulation would result in sidebands down by more than 20 dB before a Hanning window, and they would be symmetrical.
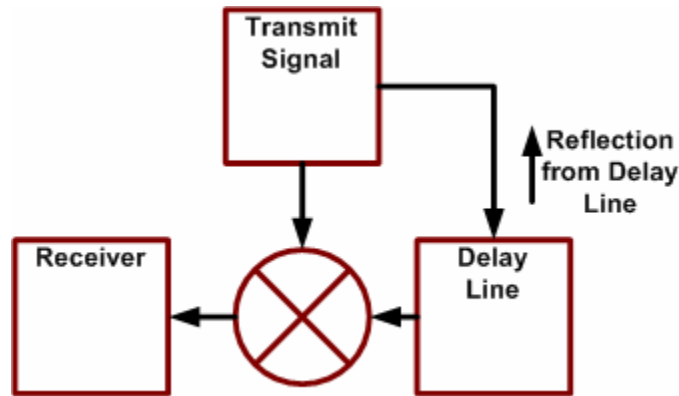

Figure 5.5: Block Diagram of Delay Line Test

With a Hanning window, they would be down even further. To test the oscillator, we took a delay line response with just the oscillator, and the result is shown in Figure 5.6. Again, we used a Hanning window. From this figure we see that the sidelobes are down by more than 28 dB, and we do not see the effect shown above in Figure 5.6 . Also, we would not expect to see the effects of phase noise and amplitude variation in this spectrum, since, with a Hanning window, they will be reduced even further. The oscillator beat spectrum by itself looks excellent, and therefore, this effect must be coming from the system. The phase response of the components of the system is very linear, so this shouldn't be causing this. A strong possibility is a multiple reflection somewhere, and a possibility is a reflection from the output port of the RF amplifier.

Figure 5.7 shows a comparison between the ideal spectrum (red), and the data with both the delay line effect removed and the system response removed. From Figure 5.7, we see that there is a close match between the two main lobes. We can calculate the resolution by finding the difference between the –3 dB frequency on one side and the frequency of the peak. We can then convert this into a resolution in distance.
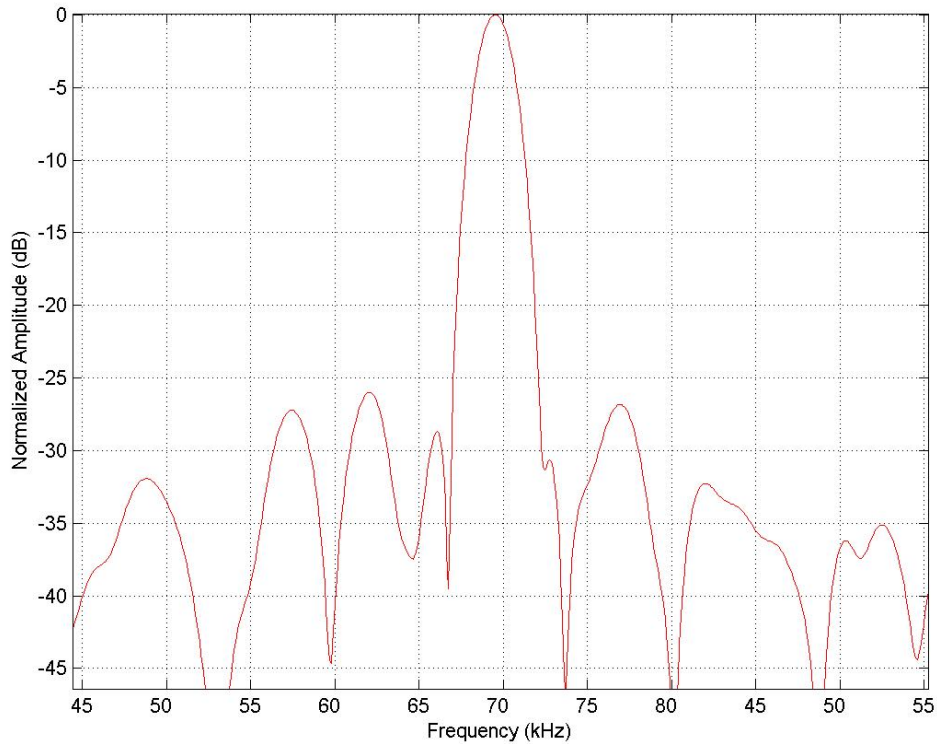

Figure 5.6 : Spectrum From Delay Line Test Using Just the Oscillator

When this is done, we obtain a resolution of 10 cm, which is the desired resolution. In this delay line response, we also see some spurious signals that are caused by multiple reflections. This causes a mismatch between the ideal response and the delay line response.

During the 2004 field season, we tested the radar over a 10 km by 10 km grid. During testing, we found that the feedthrough power from the transmit antenna to the

receive antenna was approximately -19 dBm. Since this would put the RF power at the mixer at approximately -1 dBm, and the LO power was 7 dBm, we needed to lower the RF feedthrough signal. Therefore, we put a 10-dB pad at the input of the receiver to lower the power from the top layers so third order products are reduced.
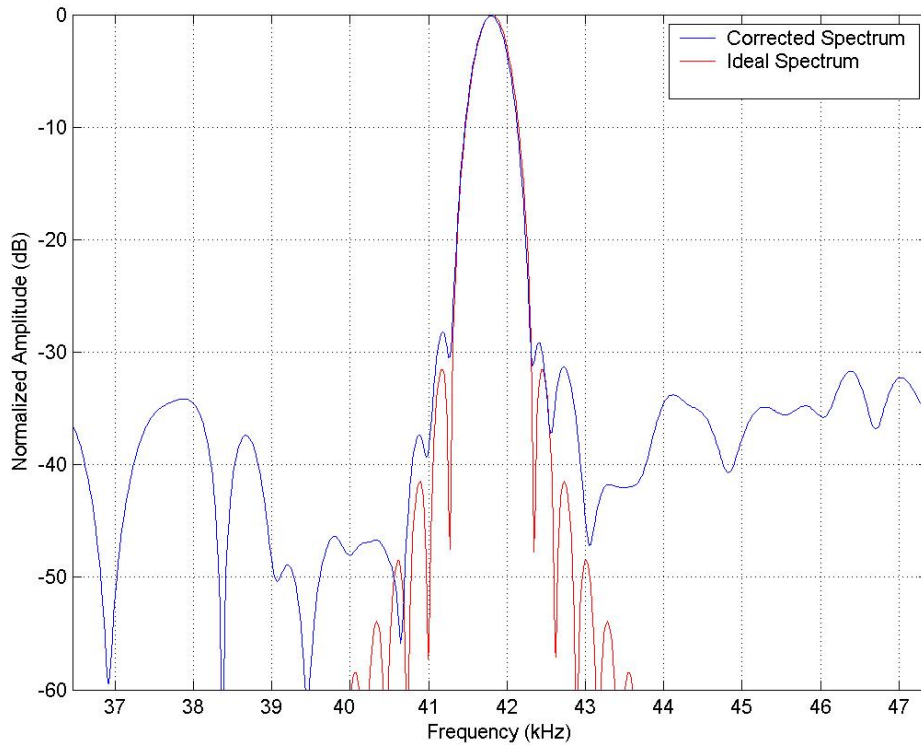

Figure 5.7: Corrected Response (Blue) vs. Ideal Response (Red)

We also tried using a 4 dB pad, but noticed extra spectral lines when compared with the 10-dB pad. Even though putting a 10-dB pad on the front added to the noise figure, we were still able to see down to 200 m, so this wasn't a problem. We also put a 3-dB pad between the transmitter and transmit antenna, to reduce multiple reflections. We collected data over 10 lines with 1 km spacing. Figures 5.8 and 5.9 show a map of part of one of the lines.

Figure 5.8 shows the top 50 m of layers in ice, while the bottom shows layers between 200 to 300 m. Figure 5.8 starts from 10 m because the length of the cables

from the transmitter and receiver were both around 4 m, and the antennas were about 2 m apart. The top layer is the feed-through signal. In Figure 5.9, we can still see layers at about 274 m. From the a-scope data, we had about 5 dB of signal-to-noise ratio at the bottom layers.
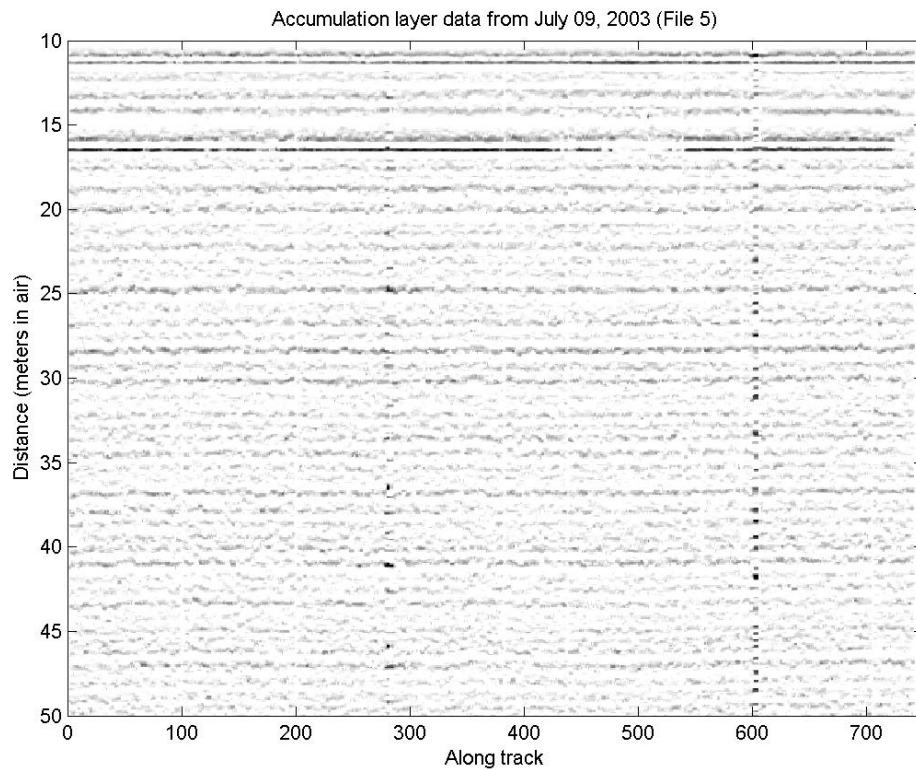

Figure 5.8: Top Internal Layers from Summit

We can analyze the data to determine the reflection coefficient from the surface and compare it with the value obtained in simulation. We need to remove the effects of the Gaussian Filter and the receiver gain in order to determine the power level at the front-end of the receiver. We removed these effects from one set of A-scope data. Additionally, the front-end to the Data Acquisition system has a transformer that has a high-pass filter response. Its 3-dB frequency is 400 kHz, and it has a 20 dB/decaderoll-off. We removed this effect as well.

We obtained the antenna gain parameters from simulation. Using Equation 3.6, we can compute the actual power reflection coefficient at 500 MHz, which is around −21 dB. Wc can compute the actual power reflection coefficient from the surface by using density information from Summit Greenland found in [27]. Using a surface density value of .321 g/cm^3, we first need to convert this to a permittivity value.
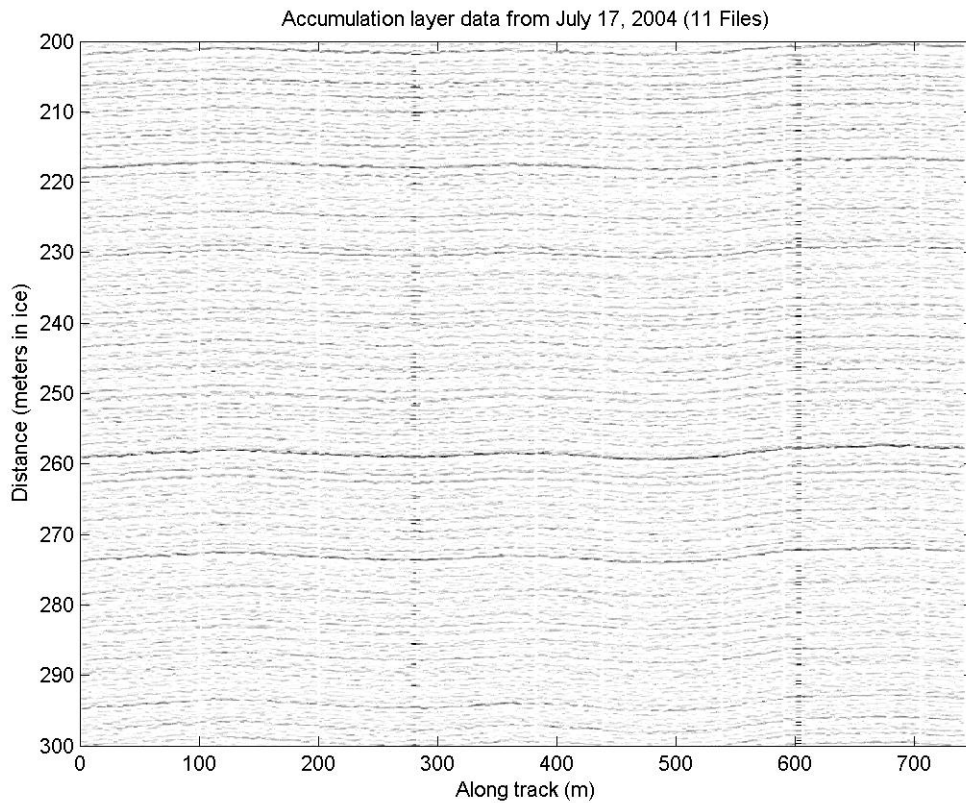
Figure 5.9: Deep Internal Layers from Summit

Using the formula in [28], we find that its permittivity is 1.62. The reflection coefficient of the air/firn interface is then found to be around −18.5 dB, which is close to the value obtained from the data.

Similar to the analysis done for NGRIP, we can estimate the water equivalent snow accumulation in Summit. In this case, there are approximately 6 layers every 5

meters, so the accumulation is approximately .8 m/year. Multiplying this by the ratio of densities as in equation 5.1, we get a value of .364 m/year for the water equivalent snow accumulation. In recent years, the average water equivalent snowfall was around .3 m/year [20], which matches favorably with our estimated value.

Additionally, we took a measurement with the antenna pointed to the sky. The thermal noise floor occurs at around 800 kHz in the beat frequency spectrum, and in the a-scope data. In Chapter 3, we calculated our MDS assuming we were limited by thermal noise. Since our MDS will come at a beat frequency of approximately 1.2 MHz, this assumption is validated, since we are in the thermal noise at 800 kHz.

CHAPTER 6

CONCLUSIONS AND RECOMMENDATIONS

The wideband accumulation radar system was designed to map the near-surface internal layers to a resolution of 10 cm, while meeting various other requirements of the PRISM project. The entire radar fits inside one CompactPCI enclosure, and is extremely lightweight. The concept of using the FM coil to phase-lock the YIG oscillator has been proven.

The hardware consists of 5 modules. The PLL board, which was used to generate the transmit signal, was designed on a four-layer FR-4 board. The AGC circuitry, which levels off the transmit power, was designed on two boards. The high-frequency section was done on a two-layer Rogers4350 board, while the low-frequency feedback section was done on a four-layer FR-4 board. The low-frequency board plugs-on to the high frequency board. The PLO section, which provides two 50 MHz signals to the data acquisition system, and the 4 GHz signal used to mix the YIG signal down to 500-to-2000 MHz, was designed on a two-layer Rogers4350 board. The receiver consists of two sections. The RF section, which filters, amplifies, and mixes down the received signal, was designed on a two-layer Rogers4350 board. The IF section, which filters and amplifies the IF signal, was designed on a two-layer FR-4 board. The main characteristics of this radar are stated below:

- Can map near-surface internal layers to a depth of 200 m

- Layering data obtained has very fine resolution

- Radar provides an extremely linear sweep

- Radar is extremely compact

It should be noted that this radar was developed with ground-based experiments in mind. Consequently, the sweep time is relatively slow (4 ms). If faster sweep times are desired, the main coil driver bandwidth will have to be increased. The loop filter will also have to be optimized, and this involves a better understanding of how the comparison frequency affects lock time, and optimizing the loop filter in general. With this YIG, the FM coil can correct for a maximum of 30 MHz deviation, and a simple simulation can determine how fast the main coil can be swept and still deviate by at most 30 MHz from perfect linearity.

BIBLIOGRAPHY

[1] Etkins, R., and E.S. Epstein, "The Rise of Global Mean Sea Level as an Indication of Climate Change", Science, vol. 215, pp. 287-289, 15 January, 1982

[2] "Warming to Cause Catastrophic Rise in Sea Level?", http://news.nationalgeographic.com/news/2004/04/0420_040420_earthday.html

[3] Bogorodsky, V.V., V.I. Pozdnynak, G.V. Trepov, and A.M. Shremet'yev, "Radar Sounding Measurements of the Thickness of Annual Snow Strata in the Antarctic", Doklady of the Academy of Sciences of the U.S.S.R. Earth science sections, vol. 264, no. 4, pp. 909-911, 1982

[4] Paterson, W.B., "The Physics of Glaciers", Butterworth-Heinemann, Oxford, England, 1982

[5] Van Der Ween, C.J., J.F. Bolzan, "Interannual Variability in Net Accumulation on the Greenland Ice Sheet: Observations and Implications for Mass Balance Measurements", Journal of Geophysical Research, vol. 104, no. D2, pp. 2009-2014, 1999

[6] "Ice Sheet Mass Balance", http://www.ume.maine.edu/iceage/Research/Contrib/html/contrib8.html

[7] Bales, R.C, J.R. McConnell, E. Mosely-Thompson, and B. Csthao, "Accumulation over the Greenland Ice Sheet from Historical and Recent Records", Journal of Geophysical Research, vol. 106, no. D24, pp. 33813-33826, 2001b

[8] Kanagaratnam, P., "Airborne Radar for High-Resolution Mapping of Internal Layers in Glacial Ice to Estimate Accumulation Rate", Ph.D. Thesis, 2002

[9] Bailey, J.T., S. Evans, and G. de Q. Robin, "Radio Echo Soundings of Polar Ice Sheets", Nature, vol. 204, pp.420-421, 1964

[10] Gogineni, S., T. Chuah, C. Allen, K. Jezek, and R.K. Moore, "An Improved Coherent Radar Depth Sounder", Journal of Glaciology, vol. 44, no. 148, 1998

[11] Hammer, C.U., "Acidity of Polar Ice Cores in Relation to Absolute Dating, Past Volcanism, and Radio-Echoes", Journal of Glaciology, vol. 25, no. 93, pp. 359-372, 1980

[12] Vickers, R.S., and G.C. Rose, "High Resolution measurements of snowpack stratigraphy using a Short Pulse Radar, Proceeding of the Eighth International Symposium on Remote Sensing of Environment", vol. 1, pp. 261-267, Ann Arbor, Michigan, October 2-6, 1972

[13] Ellerbruch, D.A., and H.S. Boyne, "Snow stratigraphy and water equivalence measured with an active microwave system", Journal of Glaciology, vol. 26, no. 94, pp. 225-233, 1980

[14] Forster, R.R., C.H. Davis, T.W. Rand, and R.K. Moore, "Snow-stratification investigations on an Antarctic ice stream with an X-band radar system", Journal of Glaciology, vol. 37, no. 127, 1991

[15] Wong, W., "Development of a Prototype of a 2-8 GHz FMCW Radar for Snow Thickness Measurement on Sea Ice", Masters Thesis, 2003

[16] Fujita, S., T. Matsuoka, T. Ishida, K. Matsuoka, and S. Mae, "A Summary of the Complex Dielectric Permittivity of Ice in the Megahertz Range and its Application for Radar Sounding of Polar Ice Sheets", Physics of Ice Core Records, ed., by T. Hondoh, pp. 185-212, Hokkaido University Press, Sapporo, Japan, 2000

[17] Griffiths, H.D., "The Effects of Phase and Amplitude Errors in FM-Radar"

[18] MLMH0208 Data Sheet, http://www.microlambdawireless.com/YIG_Oscillators/EMYTOs/MLMH_Series_HighSpeed_VXI_VME.htm

[19] Kanagaratnam, P. Private Communication, Lawrence, KS, 2002-2004

[20] http://www.ume.maine.edu/GISP2/DATA/Accum.html

[21] Kuchikulla, Abhinay, "Design and Development of a Wideband Coherent Radar Depth Sounder", Masters Thesis, 2004

[22] Curtin, Mike, and Paul O'Brien, "Phase-Locked Loops for High-Frequency Receivers and Transmitters", Analog Dialogue, Vol. 33, Number 5, May, 1999

[23] Ramasami, V. Private Communication, Lawrence, KS, 2004

[24] Castetter, Dave, "An Introduction to YIG Tuned Oscillators", MicroSource, INC., http://www.microsource-inc.com/yigintro.pdf

[25] Texas Instruments Data Book, "Noise Analysis in Operational Amplifier" Circuits, Texas Instruments Incorporated, 2000

[26] de Wit, J.J.M, and P. Hoogeboom, "High Resolution FM-CW SAR Performance Analysis"

[27] Bolzan, J., and M. Strobel, "Accumulation-rate variations around Summit, Greenland," Journal of Glaciology, vol. 40, pp. 56-66, 1994. Data archived at the World Data Center for Paleoclimatology, Boulder, Colorado, USA.